

SHAPE OPTIMIZATION OF SLIP-DRIVEN AXISYMMETRIC
MICROSWIMMERS*RUOWEN LIU[†], HAI ZHU[‡], HANLIANG GUO[§], MARC BONNET[¶], AND
SHRAVAN VEERAPANENI^{||}

Abstract. In this work, we develop a computational framework that aims at simultaneously optimizing the shape and the slip velocity of an axisymmetric microswimmer suspended in a viscous fluid. We consider shapes of a given reduced volume that maximize the swimming efficiency, i.e., the (size-independent) ratio of the power loss arising from towing the rigid body of the same shape and size at the same translation velocity to the actual power loss incurred by swimming via the slip velocity. The optimal slip and efficiency (with shape fixed) are here given in terms of two Stokes flow solutions, and we then establish shape sensitivity formulas of adjoint-solution that provide objective function derivatives with respect to any set of shape parameters on the sole basis of the above two flow solutions. Our computational treatment relies on a fast and accurate boundary integral solver for solving all Stokes flow problems. We validate our analytic shape derivative formulas via comparisons against finite-difference gradient evaluations and present several shape optimization examples.

Key words. low-Reynolds locomotion, shape sensitivity analysis, integral equations, fast algorithms

MSC codes. 49M41, 76D07, 65N38

DOI. 10.1137/24M1659649



See reproducibility of
computational results
at end of the article.

1. Introduction. Studying the efficiency of biological microswimmers is pivotal to understanding natural systems and designing artificial ones for accomplishing various physical tasks [10]. Both the body shape and the locomotory gait contribute to the swimming efficiency of the microswimmers. However, since the inertial effects are negligible at the microscale, optimal swimming strategies markedly diverge from those observed at larger scales (e.g., swimming of fish) [16]. Additionally, many microswimmers are covered by densely packed cilia, which are active microtubule-based structures much shorter than the microswimmer’s body size [8]. The periodic beatings of cilia turn the cell surface into an “active slip surface” without much change to the body shape (see, e.g., [3] and [24]). As a result, naively finding the swimmer shape to minimize the fluid drag could be a suboptimal strategy. On the other hand, artificial microswimmers such as phoretic particles locomote by the effective slip velocities on the particle surfaces resulting from the asymmetry of chemical reactions on their surfaces [2, 11, 22]. Artificial microswimmers have attracted much attention, owing to their importance in applications such as targeted drug delivery, microsurgery, and automated transport of cargo/payloads in microfluidic chips [18]. Consequently,

*Submitted to the journal’s Numerical Algorithms for Scientific Computing section May 7, 2024; accepted for publication (in revised form) October 30, 2024; published electronically April 8, 2025.

<https://doi.org/10.1137/24M1659649>

Funding: We acknowledge support from the NSF under grants DMS-1454010 and DMS-2012424

[†]Department of Mathematics, Rider University, Lawrenceville, NJ 08648 USA (rliu@rider.edu).

[‡]Flatiron Institute, Simons Foundation, New York, NY 10010 USA (hzhu@flatironinstitute.org).

[§]Department of Mathematics & Computer Science, Ohio Wesleyan University, Delaware, OH 43015 USA (hguo@owu.edu).

[¶]POEMS (CNRS, INRIA, ENSTA), ENSTA Paris, 91120 Palaiseau, France (mbonnet@ensta.fr).

^{||}Department of Mathematics, University of Michigan, Ann Arbor, MI 48109 USA (shravan@umich.edu).

shape optimization for the slip-driven microswimmers can shed light on the shapes and swimming mechanisms of biological microswimmers and provide guidance for the design and engineering of artificial ones.

In an earlier work, the authors of [17] studied the optimal slip velocity of spheroids, using analytical solutions of the Stokes equations in spheroidal coordinates. In contrast to the drag minimization problem where optimal shapes provide marginal efficiency gains over spheroids [25, 6, 21], they found that the swimming efficiency grows unbounded with the aspect ratio. Shortly after, the author of [27] optimized the shape and slip velocity for swimming efficiency at the same time, subject to a minimum curvature constraint. Motivated by the cilia carpet that formed the slip surface, the author considered the energy dissipation *inside* the cilia carpet, and assumed a local linear relationship between slip velocity and force density, which simplified the question significantly to a quadratic problem. The optimal shapes with different minimum curvatures evolve from a sphere to a prolate shape with ripples on the surface and eventually to American football shape with long protrusions from both ends as the allowed minimum curvature decreases from one to almost zero. The activation (slip velocity) of the protruded shape appears to be heavily localized near the ends of the protrusions.

In a recent study [13], we introduced a numerical algorithm for determining, for a given arbitrary axisymmetric shape, the slip velocity that minimizes the power loss *outside* the slip surface while maintaining a given swim speed. By exploiting the quadratic dependence in the slip velocity of the power loss functional, the numerical solution of the resulting optimization problem could be performed efficiently with the help of a fast boundary integral solver for the forward problem, typically taking only a few seconds on a standard laptop for a given shape [13]. We explored a wide range of shapes with different reduced volume (volume normalized by surface area) and found prolate spheroids to be the most efficient among the tested shapes.

In this work, we develop a computational framework for the joint optimization of the shape and the slip velocity subject to the volume and the surface area being constant. While our main focus is on the shape optimization component, we also provide an improved version of our earlier slip optimization method [13], whereby the optimal slip velocity and swim efficiency are obtained for a given fixed shape in terms of just two flow solutions. The main contributions of this work are two-fold. First, we establish shape sensitivity formulas tailored to the specific characteristics of the problem at hand. Their derivation exploits the fact that the swimming efficiency is given for any shape by a Rayleigh quotient of quadratic forms and uses the weak formulation of the flow problems together with reciprocity identities. The resulting shape sensitivities are expressed as integrals on the swimmer boundary involving the two solutions that determine the optimal slip and in a form consistent with the general structure of shape derivative formulas [14]. They conform to the widely used adjoint solution approach [15], as it allows one to evaluate shape functional derivatives with respect to any chosen set of shape parameters on the basis of only the two aforementioned flow solutions. Second, as in [4, 5], we employ boundary integral equation (BIE) techniques to solve the flow problems in a straightforward manner. For shape optimization problems, BIEs have the significant advantage of avoiding any volume remeshing between optimization iterations, on top of other usual advantages over classical domain discretization methods. An additional contribution lies in the improved version of the slip optimization component given in this work, whose role is important for the combined optimization problem at hand since the same two flow solutions provide the optimal slip as well as all shape sensitivities on any given shape. While the

combination of adjoint-solution and BIE methods have been successfully applied to shape optimization problems for Stokes flow previously (see, e.g., [29, 1, 28, 4, 5]), we are not aware of any work that applied these methods to slip-driven microswimmers.

The paper is organized as follows. We introduce the underlying forward problem in section 2, and then we formulate the optimization problem and derive the sensitivity formulas in section 3. The proof of the main shape sensitivity results is then given in section 3.5. We next propose the numerical scheme in section 4 and provide some numerical examples in section 5. Section 6 closes the paper with concluding remarks.

2. Forward problem formulation.

2.1. Geometry and notation. Let the axisymmetric body of the microswimmer occupy the bounded domain Ω_s with (closed smooth) boundary $\partial\Omega_s = \Gamma$, and let $\Omega = \mathbb{R}^3 \setminus \overline{\Omega}_s$ denote the unbounded fluid region surrounding it. The surface Γ is generated by rotating about e_z an open arc γ given in the (e_x, e_z) -plane by

$$\gamma \ni \mathbf{x}_\gamma(t) = R(t)e_x + Z(t)e_z, \quad 0 \leq t \leq \pi,$$

where the parametric interval $t \in [0, \pi]$ is used for consistency with the implementation (see Figure 1.1) and R, Z are smooth (C^2) functions satisfying

$$(2.1) \quad (a) \quad R(0) = R(\pi) = 0, \quad (b) \quad R(t) \geq 0, \quad (c) \quad Z'(0) = Z'(\pi) = 0$$

(the prime symbol $()'$ indicating derivatives of univariate functions). The last condition above ensures that Γ is smooth at the poles. The surface Γ then has the parametric representation

$$(2.2) \quad \Gamma \ni \mathbf{x}(t, \phi) = R(t)e_r(\phi) + Z(t)e_z, \quad 0 \leq t \leq \pi, \quad 0 \leq \phi < 2\pi,$$

where ϕ denotes the angular polar coordinate in the (e_x, e_y) -plane and $e_r(\phi) = e_x \cos \phi + e_y \sin \phi$. The unit tangent vector $\tau(t, \phi)$ in the meridian (e_r, e_z) -plane and the unit normal vector $n(t, \phi)$ pointing inwards of the body are given by

$$(2.3) \quad \alpha(t)\tau(t, \phi) = R'(t)e_r(\phi) + Z'(t)e_z, \quad \alpha(t)n(t, \phi) = Z'(t)e_r(\phi) - R'(t)e_z,$$

where $\alpha(t) := \sqrt{R'^2(t) + Z'^2(t)}$ is the arc-length Jacobian. Any axisymmetric vector field \mathbf{v} on Γ has the form

$$(2.4) \quad \begin{aligned} \mathbf{v}(t, \phi) &= v_\tau(t)\tau(t, \phi) + v_n(t)n(t, \phi) \\ \text{with } v_\tau &:= \mathbf{v} \cdot \tau, \quad v_n := \mathbf{v} \cdot n, \quad 0 \leq t \leq \pi, \quad 0 \leq \phi < 2\pi, \end{aligned}$$

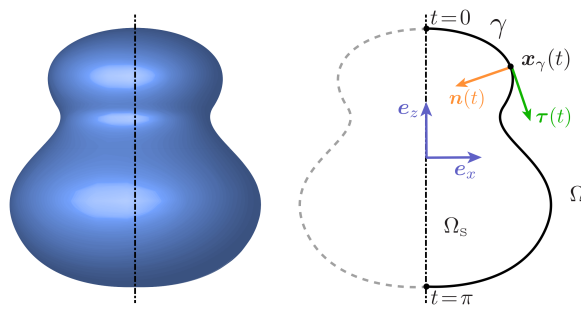


FIG. 1.1. Axisymmetric body of the microswimmer: geometry and notation.

which will often be used in what follows. Then, by the Frenet formulas on γ_ϕ ,

$$(2.5) \quad \begin{aligned} \partial_t \mathbf{x}(t, \phi) &= \alpha(t) \boldsymbol{\tau}(t, \phi), \\ \partial_t \boldsymbol{\tau}(t, \phi) &= \alpha(t) \kappa(t) \mathbf{n}(t, \phi), \quad \partial_t \mathbf{n}(t, \phi) = -\alpha(t) \kappa(t) \boldsymbol{\tau}(t, \phi), \end{aligned}$$

where $\kappa = \kappa(t)$ is the curvature, given by $\alpha^3 \kappa = \alpha^2 \mathbf{n} \cdot \partial_t \boldsymbol{\tau} = -\alpha^2 \boldsymbol{\tau} \cdot \partial_t \mathbf{n} = Z' R'' - R' Z''$. The differential area element on Γ is $dS = R(t) \alpha(t) dt d\phi$. For any axisymmetric function f defined on Γ , we have

$$(2.6) \quad \int_{\Gamma} f dS = \int_0^{2\pi} \int_0^\pi f(t) R(t) \alpha(t) dt d\phi = 2\pi \int_0^\pi f(t) R(t) \alpha(t) dt.$$

2.2. PDE of forward problem.

Axisymmetric slip velocities are of the form

$$\mathbf{u}^s(t, \phi) = u^s(t) \boldsymbol{\tau}(t, \phi)$$

at any point $\mathbf{x}(t, \phi) \in \Gamma$, where $u^s(t)$ is the slip velocity profile and the unit tangent $\boldsymbol{\tau}$ is defined by (2.3). The axisymmetry assumption also implies that $u^s(t)$ must satisfy

$$(2.7) \quad u^s(0) = u^s(\pi) = 0$$

to prevent singularities in the flow problem. In the viscous dominant regime, the velocity field \mathbf{u} and the pressure field p in the fluid region verify the Stokes PDE system

$$(2.8) \quad -\mu \nabla^2 \mathbf{u} + \nabla p = \mathbf{0}, \quad \nabla \cdot \mathbf{u} = 0 \quad \forall \mathbf{x} \in \Omega,$$

where μ is the dynamic viscosity. In addition, the velocity is prescribed on Γ as

$$(2.9) \quad \mathbf{u} = \mathbf{u}^D := U \mathbf{e}_z + u^s \boldsymbol{\tau} \quad \text{on } \Gamma,$$

where the axial (along the z -axis) translation velocity U of the body is determined by requiring that the force density

$$(2.10) \quad \mathbf{f} = -p \mathbf{n} + 2\mu \mathbf{D}[\mathbf{u}] \quad \text{with} \quad \mathbf{D}[\mathbf{u}] := \frac{1}{2} (\nabla \mathbf{u} + \nabla^T \mathbf{u})$$

induced by the flow produces a zero axial net force, i.e.,

$$(2.11) \quad 0 = \langle \mathbf{f}, \mathbf{e}_z \rangle_{\Gamma} = \int_{\Gamma} (\mathbf{f} \cdot \mathbf{e}_z) dS = 2\pi \int_0^\pi (\mathbf{f}(t) \cdot \mathbf{e}_z) R(t) \alpha(t) dt,$$

where $\langle \cdot, \cdot \rangle_{\Gamma}$ stands for the $L^2(\Gamma)$ duality product and having used (2.6). Both the geometry and the slip velocity being (by assumption) axisymmetric, so is the flow, which prevents rigid-body motions other than axial translations and implies automatic satisfaction of the no-net-torque and remaining no-net-force conditions.

We record the following sign and reciprocity properties.

LEMMA 2.1. *Let $(\mathbf{u}, p, \mathbf{f})$ solve problem (2.8)–(2.9). Then*

$$\langle \mathbf{u}^D, \mathbf{f} \rangle_{\Gamma} = a(\mathbf{u}, \mathbf{u}) \geq 0,$$

where the positive bilinear form $a(\cdot, \cdot)$ is associated with the weak form of (2.8)–(2.9) (see section 3.5) and defined by (3.29). In addition, let $(\mathbf{u}_1, p_1, \mathbf{f}_1)$ define another solution of (2.8)–(2.9) with prescribed velocity $\mathbf{u}_1^D = U_1 \mathbf{e}_z + u_1^s \boldsymbol{\tau}$. Then

$$\langle \mathbf{u}_1^D, \mathbf{f} \rangle_{\Gamma} = \langle \mathbf{u}^D, \mathbf{f}_1 \rangle_{\Gamma}.$$

Proof. For the sign property, write (3.29) for $(\mathbf{v}, q, \mathbf{g}) = (\mathbf{u}, p, \mathbf{f})$ and recall that $\nabla \cdot \mathbf{u} = 0$. For the reciprocity property, write (3.29) for $(\mathbf{v}, q, \mathbf{g}) = (\mathbf{u}_1, p_1, \mathbf{f}_1)$ and the similar identity obtained by reversing the roles of the two solutions, subtract the resulting equalities, and use the symmetry property $a(\mathbf{u}, \mathbf{u}_1) = a(\mathbf{u}_1, \mathbf{u})$. \square

We also introduce the solution $(\hat{\mathbf{u}}, \hat{p}, \hat{\mathbf{f}})$ of the rigid-body translation problem

$$(2.12) \quad (a) \quad -\mu \nabla^2 \hat{\mathbf{u}} + \nabla \hat{p} = \mathbf{0}, \quad \nabla \cdot \hat{\mathbf{u}} = 0 \quad \text{in } \Omega, \quad (b) \quad \hat{\mathbf{u}} = \mathbf{e}_z \quad \text{on } \Gamma,$$

i.e., problem (2.8)–(2.9) with $(U, u^s) = (1, 0)$ governing the flow created by towing the rigid-body Ω at an unit axial speed. We then have

$$\mathbf{f}[u^s] = \mathbf{f}_0[u^s] + U(u^s, \Gamma)\hat{\mathbf{f}},$$

where $\mathbf{f}_0[u^s]$ denotes the traction associated with the solution of problem (2.8)–(2.9) with $U = 0$. Using the reciprocity property of Lemma 2.1, the no-net-force condition (2.11) reads as

$$(2.13) \quad 0 = F_0(\Gamma)U(u^s, \Gamma) + \langle \mathbf{f}_0[u^s], \mathbf{e}_z \rangle_{\Gamma} = F_0(\Gamma)U(u^s, \Gamma) + \langle \hat{\mathbf{f}}_{\tau}, u^s \rangle_{\Gamma},$$

where $\hat{\mathbf{f}}_{\tau} := \hat{\mathbf{f}} \cdot \boldsymbol{\tau}$ by the convention (2.4) and the drag coefficient $F_0(\Gamma)$, given by

$$(2.14) \quad F_0(\Gamma) = \langle \hat{\mathbf{f}}, \mathbf{e}_z \rangle_{\Gamma},$$

is the net force incurred by towing the rigid body at a unit axial speed.

3. Optimization problems and shape sensitivity analysis. Our aim is to find an optimal shape Γ achieving low-Reynolds locomotion with maximum swimming efficiency. Following [19], the swimming efficiency of the body is defined as

$$(3.1) \quad J_E(u^s, \Gamma) := \frac{J_D(u^s, \Gamma)}{J_W(u^s, \Gamma)},$$

where

$$(3.2) \quad J_W(u^s, \Gamma) := \langle \mathbf{f}[u^s], \mathbf{u}^D \rangle_{\Gamma} = \langle f_{\tau}, u^s \rangle_{\Gamma}$$

is the power dissipated in the actual motion described by (2.8)–(2.11) (with the second equality stemming from (2.9) and (2.11)) and

$$(3.3) \quad J_D(u^s, \Gamma) := F_0(\Gamma)U^2(u^s, \Gamma)$$

is the power loss caused by towing a rigid body of the same shape at the axial translation velocity $U = U(u^s, \Gamma)$. Applying the sign property of Lemma 2.1 to (3.2) and (2.14), we deduce $J_W(u^s, \Gamma) \geq 0$ and $F_0(\Gamma) \geq 0$ for any Γ, u^s . As a result, the swimming efficiency (3.1) takes the form

$$(3.4) \quad J_E(u^s, \Gamma) = \frac{A_D(u^s, u^s, \Gamma)}{A_W(u^s, u^s, \Gamma)}$$

with the positive bilinear forms A_D and A_W given by

$$(3.5) \quad A_D(u^s, w^s, \Gamma) = \langle \hat{\mathbf{f}}_{\tau}, u^s \rangle_{\Gamma} \langle \hat{\mathbf{f}}_{\tau}, w^s \rangle_{\Gamma}, \quad A_W(u^s, w^s, \Gamma) = F_0(\Gamma) \langle f_{\tau}[u^s], w^s \rangle_{\Gamma}.$$

3.1. Optimization problems. Our main goal is to solve numerically the optimization problem

$$(3.6) \quad \max_{u^s, \Gamma} J_E(u^s, \Gamma) \quad \text{subject to} \quad C_\nu(\Gamma) := \nu(\Gamma) - \nu_0 = 0,$$

where the swimming efficiency is to be maximized with respect to both the applied slip velocity profile u^s and the body shape Γ , subject to the reduced volume

$$(3.7) \quad \nu(\Gamma) := 6\sqrt{\pi}V/A^{3/2}$$

having a prescribed value ν_0 (with $V = |\Omega_S|$ and $A = |\Gamma|$ the volume and surface area of the microswimmer). We note that the reduced volume is a function of the swimmer's shape, but not of its size, since scaling the swimmer uniformly in all directions does not change $\nu(\Gamma)$. Additionally, we have $\nu(\Gamma) \leq 1$ for all shapes, and $\nu(\Gamma) = 1$ if and only if Γ is a sphere.

To solve problem (3.6), we take advantage of an available solution method for the partial maximization of $J_E(u^s, \Gamma)$ with fixed shape; see section 3.2. We thus define

$$(3.8) \quad E(\Gamma) := \max_{u^s} J_E(u^s, \Gamma)$$

and note that $E(\Gamma)$ is a shape functional since its value is entirely determined by Γ . We then recast the joint optimization problem (3.6) as the constrained shape optimization problem

$$(3.9) \quad \max_{\Gamma} E(\Gamma) \quad \text{subject to} \quad C_\nu(\Gamma) = 0.$$

The equality constraint will be handled using the augmented Lagrangian method (ALM) described in section 4.3, the constrained problem (3.9) thus being treated as a sequence of unconstrained problems.

We will also consider, for comparison purposes, the constrained shape optimization problem

$$(3.10) \quad \min_{\Gamma} J_{\text{drag}}(\Gamma) \quad \text{subject to} \quad \nu(\Gamma) - \nu_0 = 0$$

for the normalized drag force $J_{\text{drag}}(\Gamma)$, which is defined by $J_{\text{drag}}(\Gamma) := F_0(\Gamma)/6\pi\mu r$ for a (passive) rigid body in Stokes flow ($r = \sqrt[3]{3V/(4\pi)}$ being the radius of the ball having the same volume V as Ω_S). It is worth noting that $J_{\text{drag}}(\Gamma)$ is dimensionless and does not depend on the size of Ω_S .

3.2. Partial optimization with fixed shape. Here we present an improved version of the method proposed in [13] for solving the slip optimization problem (3.8) with a fixed shape Γ . This step exploits the fact that $J_E(u^s, \Gamma)$ is, for given Γ , expressed by (3.4) as a Rayleigh quotient, so that its maximum value is equal to the largest (positive) eigenvalue of the symmetric generalized eigenvalue problem

$$(3.11) \quad \begin{aligned} &\text{Find } z^s \in H^{1/2}(\Gamma), \lambda \in \mathbb{R} \\ &\text{such that} \quad A_D(z^s, w^s, \Gamma) - \lambda A_W(z^s, w^s, \Gamma) = 0 \quad \text{for all } w^s \in H^{1/2}(\Gamma), \end{aligned}$$

the corresponding eigenfunction z^s defining a slip velocity profile producing the optimal efficiency. Problem (3.11) turns out to be easy to solve: since the bilinear form A_D is of rank one (while A_W is positive definite), there is only one nonzero eigenvalue $\lambda > 0$, whose multiplicity is 1.

Let the fields $(\tilde{\mathbf{u}}, \tilde{p})$ solve the axisymmetric Stokes flow problem

$$(3.12) \quad \begin{aligned} \text{(a)} \quad & -\mu \nabla^2 \tilde{\mathbf{u}} + \nabla \tilde{p} = \mathbf{0}, \quad \nabla \cdot \tilde{\mathbf{u}} = 0, \quad \text{in } \Omega, \\ \text{(b)} \quad & \tilde{\mathbf{f}} \cdot \boldsymbol{\tau} = \hat{\mathbf{f}} \cdot \boldsymbol{\tau}, \\ \text{(c)} \quad & \tilde{\mathbf{u}} \cdot \mathbf{n} = 0 \quad \text{on } \Gamma, \end{aligned}$$

where $\tilde{\mathbf{f}}$ is the traction vector associated with $(\tilde{\mathbf{u}}, \tilde{p})$. Using the above solution, the slip velocity defined by

$$(3.13) \quad z^s := \tilde{\mathbf{u}} \cdot \boldsymbol{\tau}$$

then yields the maximal swimming efficiency for a fixed shape Γ .

PROPOSITION 3.1. *The slip velocity profile z^s defined for a given shape Γ by (3.13) in terms of the solution of problem (3.12) solves the partial maximization problem (3.8): we have*

$$(3.14) \quad z^s = \arg \max_{u^s} J_E(u^s, \Gamma), \quad E(\Gamma) = -\frac{U(z^s, \Gamma)}{1 + U(z^s, \Gamma)} \geq 0.$$

Proof. Let z^s be given by (3.13). Using (2.13) and (3.27) in (3.5), we have

$$\begin{aligned} A_D(z^s, w^s, \Gamma) &= \langle \hat{\mathbf{f}}_\tau, z^s \rangle_\Gamma \langle \hat{\mathbf{f}}_\tau, w^s \rangle_\Gamma = -F_0(\Gamma)U(z^s, \Gamma)\langle \hat{\mathbf{f}}_\tau, w^s \rangle_\Gamma, \\ A_W(z^s, w^s, \Gamma) &= F_0(\Gamma)\langle f_\tau[z^s], w^s \rangle_\Gamma = F_0(\Gamma)(1 + U(z^s, \Gamma))\langle \hat{\mathbf{f}}_\tau, w^s \rangle_\Gamma. \end{aligned}$$

The eigenvalue equation (3.11) is therefore verified by z^s and $\lambda = E(\Gamma)$ given by (3.14). Since problem (3.11) has only one nonzero eigenvalue, the pair (z^s, λ) provides the maximal swimming efficiency for given Γ . \square

The treatment given in [13] needs the solution of one flow problem per basis function of the finite-dimensional approximation of u^s (see section 4.2), while the present version replaces this task with solving only (3.12) (the solution of the adjoint problem (2.12) being needed in both versions).

3.3. Shape sensitivity analysis. In this section, we collect available shape derivative concepts that fit the present needs. Rigorous expositions of shape sensitivity theory are available in [14, Chap. 5] and other monographs. Let Ω_A denote a fixed domain chosen so that $\Omega \Subset \Omega_A$ always holds for the shape optimization problem of interest. Shape changes are described with the help of transformation velocity fields, i.e., vector fields $\boldsymbol{\theta} : \Omega_A \rightarrow \mathbb{R}^3$ such that $\boldsymbol{\theta} = \mathbf{0}$ in a neighborhood of $\partial\Omega_A$; we then extend $\boldsymbol{\theta}$ by zero in $\mathbb{R}^3 \setminus \overline{\Omega}_A$. Shape perturbations of the body boundary can, in the present context, be mathematically described using a pseudo-time η and a geometrical transform of the form

$$(3.15) \quad \mathbb{R}^3 \ni \mathbf{x}(t, \phi) \mapsto \mathbf{x}_\eta(t, \phi) = \mathbf{x}(t, \phi) + \eta \boldsymbol{\theta}(t, \phi), \quad 0 \leq t \leq \pi, \quad 0 \leq \phi < 2\pi.$$

They allow one to define a parametrized family of domains $\Omega_\eta(\boldsymbol{\theta}) := (\mathbf{I} + \eta \boldsymbol{\theta})(\Omega)$ for any given “initial” domain Ω . The affine format (3.15) is sufficient for defining first-order derivatives at $\eta = 0$. In this work, perturbations $\Gamma_\eta(\boldsymbol{\theta})$ of an axisymmetric surface Γ are assumed to be defined by

$$\Gamma_\eta(\boldsymbol{\theta}) \ni \mathbf{x}_\eta(t, \phi) = \mathbf{x}(t, \phi) + \eta \boldsymbol{\theta}(t, \phi), \quad 0 \leq t \leq \pi, \quad 0 \leq \phi < 2\pi$$

in terms of axisymmetry-preserving transformation velocity fields $\boldsymbol{\theta}$ having the form

$$\boldsymbol{\theta}(t, \phi) = \theta_\tau(t) \boldsymbol{\tau}(t, \phi) + \theta_n(t) \mathbf{n}(t, \phi), \quad 0 \leq t \leq \pi, \quad 0 \leq \phi < 2\pi$$

on Γ (see (2.4)) with $\boldsymbol{\tau}$ and \mathbf{n} given by (2.3) and the components θ_τ, θ_n satisfying

$$(3.16) \quad (\text{a}) \quad \theta_\tau(0) = \theta_\tau(\pi) = 0, \quad (\text{b}) \quad \theta'_n(0) = \theta'_n(\pi) = 0.$$

The requirement (3.16)(a) ensures that Γ_η remains closed (by precluding “tearing” at the poles), and the smoothness of $\Gamma_\eta(\boldsymbol{\theta})$ at the poles is maintained by (3.16)(b). Perturbed domains $\Omega_\eta(\boldsymbol{\theta}) = (\mathbf{I} + \eta\boldsymbol{\theta})(\Omega)$ with boundary $\Gamma_\eta(\boldsymbol{\theta})$ can then be defined using arbitrary extensions of $\boldsymbol{\theta}$ to Ω .

All derivatives are implicitly taken at some given configuration Ω , i.e., at initial “time” $\eta = 0$. The “initial” material derivative $\dot{\mathbf{a}}$ of some (scalar- or tensor-valued) field variable $\mathbf{a}(\mathbf{x}, \eta)$ is defined as

$$\dot{\mathbf{a}}(\mathbf{x}) = \lim_{\eta \rightarrow 0} \frac{1}{\eta} (\mathbf{a}(\mathbf{x}_\eta, \eta) - \mathbf{a}(\mathbf{x}, 0)), \quad \mathbf{x} \in \Omega,$$

and the material derivative of gradients and divergences of tensor fields are given by

$$(3.17) \quad (\text{a}) \quad (\nabla \mathbf{a})^* = \nabla \dot{\mathbf{a}} - \nabla \mathbf{a} \cdot \nabla \boldsymbol{\theta}, \quad (\text{b}) \quad (\nabla \cdot \mathbf{a})^* = \nabla \cdot \dot{\mathbf{a}} - \nabla \mathbf{a} : \nabla \boldsymbol{\theta}.$$

Likewise, the first-order “initial” derivative J' of a shape functional J is defined as

$$J'(\Omega; \boldsymbol{\theta}) = \lim_{\eta \rightarrow 0} \frac{1}{\eta} (J(\Omega_\eta(\boldsymbol{\theta})) - J(\Omega)),$$

and its practical evaluation relies on the fact that the derivatives of generic integrals

$$(\text{a}) \quad I_V(\eta) = \int_{\Omega_\eta(\boldsymbol{\theta})} F(\cdot, \eta) dV, \quad (\text{b}) \quad I_S(\eta) = \int_{\Gamma_\eta(\boldsymbol{\theta})} F(\cdot, \eta) dS$$

on variable domains or surfaces are given by the material differentiation identities

$$(3.18) \quad \begin{aligned} (\text{a}) \quad & \left. \frac{dI_V}{d\eta} \right|_{\eta=0} = \int_{\Omega} [\dot{F} + F(\cdot, 0) \nabla \cdot \boldsymbol{\theta}] dV, \\ (\text{b}) \quad & \left. \frac{dI_S}{d\eta} \right|_{\eta=0} = \int_{\Gamma} [\dot{F} + F(\cdot, 0) \operatorname{div}_S \boldsymbol{\theta}] dS \end{aligned}$$

with the surface divergence $\operatorname{div}_S \boldsymbol{\theta}$ in (3.18)(b) given by (C.2) in Appendix C.

The *structure theorem for shape derivatives* (see, e.g., [14, sect. 5.9]) states that the shape derivative of any shape functional can be expressed as a linear functional in the normal transformation velocity θ_n . This result conforms to intuitive geometrical facts: (i) the shape of $\Omega_\eta(\boldsymbol{\theta})$ is determined by that of $\Gamma_\eta(\boldsymbol{\theta})$, and (ii) tangential components of $\boldsymbol{\theta}$ leave Ω unchanged at leading order $O(\eta)$. Here we provide, as an example and for later reference, the derivative of the reduced volume (3.7), which is a shape functional.

PROPOSITION 3.2. *The shape derivative of the reduced volume $\nu(\Gamma)$ defined by (3.7) is given by*

$$\frac{\nu'(\Gamma; \boldsymbol{\theta})}{\nu(\Gamma)} = \frac{V'(\Gamma; \boldsymbol{\theta})}{V} - \frac{3A'(\Gamma; \boldsymbol{\theta})}{2A}$$

with the shape derivatives of the volume $V = |\Omega_s|$ and area $A = |\Gamma|$ given (as linear functionals on θ_n) by

$$\begin{aligned} V'(\Gamma; \boldsymbol{\theta}) &= - \int_{\Gamma} \theta_n dS = -2\pi \int_0^\pi \theta_n R\alpha dt, \\ A'(\Gamma; \boldsymbol{\theta}) &= \int_{\Gamma} \operatorname{div}_S \boldsymbol{\theta} dS = 2\pi \int_0^\pi (Z' - \kappa R\alpha) \theta_n dt. \end{aligned}$$

For A' , we have used (C.2) and the fact that $\int_0^\pi (R\theta_\tau)' dt = 0$ due to (3.16)(a).

3.4. Shape sensitivities of swimming efficiency and normalized drag force. We begin by expressing the shape derivative of the swimming efficiency in terms of shape sensitivities of the power loss functionals.

LEMMA 3.3. *The shape derivative of $E(\Gamma)$ is given by*

$$E'(\Gamma; \boldsymbol{\theta}) = \frac{J'_D(z^s, \Gamma; \boldsymbol{\theta}) - E(\Gamma)J'_W(z^s, \Gamma; \boldsymbol{\theta})}{J_W(z^s, \Gamma)},$$

where $E(\Gamma)$ and the shape derivatives J'_W and $J'_D = [F_0 U^2]'$ are taken with the slip velocity z^s given in (3.13) (kept fixed to its optimum value at current Γ).

Proof. The maximal efficiency $E(\Gamma)$ and associated optimal slip velocity z^s at any given Γ are related through (3.11), i.e.,

$$(3.19) \quad A_D(z^s, w^s, \Gamma) - E(\Gamma)A_W(z^s, w^s, \Gamma) = 0$$

for any shape perturbation about the current shape Γ . The shape derivative at Γ of (3.19) thus yields

$$(3.20) \quad \begin{aligned} & A_D(\dot{z}^s, w^s, \Gamma) - E(\Gamma)A_W(\dot{z}^s, w^s, \Gamma) + A'_D(z^s, w^s, \Gamma; \boldsymbol{\theta}) \\ & - E(\Gamma)A'_W(z^s, w^s, \Gamma; \boldsymbol{\theta}) - E'(\Gamma; \boldsymbol{\theta})A_W(z^s, w^s, \Gamma) = 0, \end{aligned}$$

where A'_D and A'_W are shape derivatives taken with z^s fixed (i.e., $\dot{z}^s = 0$), while as usual $\dot{w}^s = 0$ may be assumed for the test functions in this derivation. Now, setting $w^s = z^s$ in the above equation and observing that the first two terms cancel due to (3.19) and the bilinear forms A_D, A_W being symmetric, we obtain

$$E'(\Gamma; \boldsymbol{\theta}) = \frac{A'_D(z^s, z^s, \Gamma; \boldsymbol{\theta}) - E(\Gamma)A'_W(z^s, z^s, \Gamma; \boldsymbol{\theta})}{A_W(z^s, z^s, \Gamma)}.$$

The claimed formula finally results from recalling the definitions (3.5) of A_D, A_W , which imply $A_D(z^s, w^s, \Gamma) = F_0(\Gamma)J_D(z^s, \Gamma)$ and $A_W(z^s, w^s, \Gamma) = F_0(\Gamma)J_W(z^s, \Gamma)$. \square

The next step then consists in deriving formulas for the shape sensitivities of the functionals involved in Lemma 3.3. The latter depend on Γ implicitly through the forward or adjoint solution. In particular, applying the material differentiation formula (3.18)(b) to (3.2) and (2.14), we have

$$(3.21) \quad J'_W(\Gamma; \boldsymbol{\theta}) = \langle \dot{\mathbf{f}}, u^s \boldsymbol{\tau} \rangle_{\Gamma} + \langle \dot{\mathbf{f}}, \mathbf{e}_z \rangle_{\Gamma} U + \langle \mathbf{f}, u^s \dot{\boldsymbol{\tau}} \rangle_{\Gamma} + \langle \mathbf{f}, (u^s \boldsymbol{\tau} + U \mathbf{e}_z) \operatorname{div}_s \boldsymbol{\theta} \rangle_{\Gamma},$$

$$(3.22) \quad F'_0(\Gamma; \boldsymbol{\theta}) = \langle \dot{\mathbf{f}}, \mathbf{e}_z \rangle_{\Gamma} + \langle \hat{\mathbf{f}}, \mathbf{e}_z \operatorname{div}_s \boldsymbol{\theta} \rangle_{\Gamma}$$

in terms of the material derivatives $\dot{\mathbf{f}}, \dot{U}$, and $\hat{\mathbf{f}}$ of solution components and $\dot{\boldsymbol{\tau}}$ of the unit tangent and having used the no-net-force identity $\langle \mathbf{f}, \mathbf{e}_z \rangle_{\Gamma} \dot{U} = 0$ for (3.21). However, as in many other similar situations, expressions of $J'_W(\Gamma; \boldsymbol{\theta})$, $F'_0(\Gamma; \boldsymbol{\theta})$, and $U'(\Gamma; \boldsymbol{\theta})$ that are free of solution derivatives can be obtained from combinations of the weak forms of the forward and derivative problems written with suitably chosen test functions. In addition, the resulting expressions are recast, using curvilinear coordinates, as boundary integrals. This somewhat lengthy process, expounded upon in section 3.5, yields the following material derivative formulas, which are free of any solution material derivative and have a form suitable for a direct implementation using the output of a BIE solver.

PROPOSITION 3.4. Consider a shape perturbation with axisymmetry-preserving transformation velocity $\boldsymbol{\theta}$, and assume the slip velocity u^s to be convected (i.e., $\dot{u}^s = 0$). The derivatives of $J_w(u^s, \Gamma)$, $U(u^s, \Gamma)$, and $F_0(\Gamma)$ are then given by

$$(3.23) \quad J'_w(u^s, \Gamma; \boldsymbol{\theta}) = 2\pi \int_0^\pi \left\{ \left[4\mu \left(\frac{R' u^s}{R\alpha} \right)^2 - \frac{1}{\mu} f_\tau^2 + \frac{1}{\mu} (f_n + p)p + 2\kappa u^s f_\tau \right] \alpha \theta_n - 2f_\tau (u^s)' \theta_\tau + 2u^s f_n \theta_n' \right\} R dt,$$

$$(3.24) \quad U'(u^s, \Gamma; \boldsymbol{\theta}) = -\frac{2\pi}{F_0} \int_0^\pi \left\{ \left[\kappa u^s \hat{f}_\tau - \frac{1}{\mu} f_\tau \hat{f}_\tau + \frac{1}{2\mu} (f_n + p)\hat{p} \right] \alpha \theta_n - \hat{f}_\tau (u^s)' \theta_\tau - u^s \hat{p} \theta_n' \right\} R dt,$$

$$(3.25) \quad F'_0(\Gamma; \boldsymbol{\theta}) = -\frac{2\pi}{\mu} \int_0^\pi \hat{f}_\tau^2 \theta_n R \alpha dt$$

with $f_\tau := \mathbf{f} \cdot \boldsymbol{\tau}$ and $f_n := \mathbf{f} \cdot \mathbf{n}$. The shape derivative of the normalized drag force is then given by

$$(3.26) \quad J'_{drag}(\Gamma; \boldsymbol{\theta}) = J_{drag}(\Gamma) \left(\frac{F'_0}{F_0} - \frac{V'}{3V} \right),$$

with V' given by Proposition 3.2.

Formulas (3.23) and (3.24) are valid for any slip velocity profile u^s that is convected by $\boldsymbol{\theta}$. Moreover, (3.23) to (3.26) are all insensitive to a perturbation of the (forward or adjoint) pressure field by a constant pressure difference Δp . For example, replacing f_n and p by $f_n - \Delta p$ and $p + \Delta p$ brings to (3.23) the additional term

$$-4\pi\Delta p \int_0^\pi [Ru^s \theta_n' + (Ru^s)' \theta_n] dt = -4\pi\Delta p \int_0^\pi (Ru^s \theta_n)' dt = 0 \quad \text{using (2.7).}$$

Applying (3.23), (3.24) with $u^s = z^s$ to Lemma 3.3 defines a computationally tractable evaluation method for the shape derivative of the swimming efficiency. We note, however, that the resulting formula for $E'(\Gamma; \boldsymbol{\theta})$ appears to involve the tangential transformation velocity θ_τ , in apparent violation of the structure theorem for shape derivatives. To resolve this contradiction, we now exploit additional properties satisfied only by the optimal slip velocity z^s . Indeed, the definition (3.13) of z^s and the boundary conditions of problems (2.8) and (2.12) together imply that $(\tilde{\mathbf{u}}, \tilde{p})$ solve problem (2.8) with $(u^s, U) = (z^s, 0)$, so that $\mathbf{f}[z^s] = \tilde{\mathbf{f}} + U(z^s, \Gamma)\hat{\mathbf{f}}$. Hence, using again the boundary condition (3.12)(b), the traction components of the forward solution are found to verify

$$(3.27) \quad \begin{aligned} f_\tau[z^s] &= \tilde{f}_\tau + U(z^s, \Gamma)\hat{f}_\tau = (1 + U(z^s, \Gamma))\hat{f}_\tau, \\ f_n[z^s] &= \tilde{f}_n - U(z^s, \Gamma)\hat{p}, \quad p[z^s] = \tilde{p} + U(z^s, \Gamma)\hat{p}. \end{aligned}$$

This results in the following final expression of the shape derivative of $E(\Gamma)$, whose form is now consistent with the structure theorem.

PROPOSITION 3.5. Let z^s be the optimal slip velocity (3.13) for given Γ , and consider a shape perturbation of Γ with axisymmetry-preserving transformation velocity field $\boldsymbol{\theta}$. The shape derivative of the optimal efficiency $E(\Gamma)$ is given by

$$(3.28) \quad E'(\Gamma; \boldsymbol{\theta}) = -\frac{2\pi}{F_0(1+U)^2} \int_0^\pi \left\{ 2z^s (\tilde{f}_n + \hat{p}) \theta'_n \right. \\ \left. + \left[4\mu \left(\frac{R' z^s}{Ra} \right)^2 + \frac{1}{\mu} (\tilde{f}_n + \tilde{p}) (\tilde{p} - \hat{p}) + \frac{1+U}{\mu} \hat{f}_\tau^2 \right] \alpha \theta_n \right\} R dt,$$

where $(\hat{\mathbf{u}}, \hat{\mathbf{f}}, \hat{p})$ and $(\tilde{\mathbf{u}}, \tilde{\mathbf{f}}, \tilde{p})$ respectively solve problems (2.12) and (3.12), $z^s = \tilde{\mathbf{u}} \cdot \boldsymbol{\tau}$, and $U = U(z^s, \Gamma)$ is given by (2.13). In particular, $E'(\Gamma; \boldsymbol{\theta})$ is a linear functional on θ_n .

Proof. We evaluate formulas (3.23) to (3.25) for the optimal slip velocity z^s , which allows us to express f_τ , f_n , and p in terms of \tilde{f}_n, \tilde{p} and \hat{f}, \hat{p} using (3.27). We then use the result to compute $E'(\Gamma; \boldsymbol{\theta})$ given by Lemma 3.3 and recall that $J_w(z^s, \Gamma) = E(\Gamma)J_D(z^s, \Gamma) = -F_0U(1+U)$ (see (3.3) and (3.14)). This yields the claimed expression of $E'(\Gamma; \boldsymbol{\theta})$. \square

3.5. Proof of Proposition 3.4.

This proof is divided into five main steps.

1. *Forward and adjoint problems in weak form.* The results of Proposition 3.4 rely on identities found by recasting the forward problem (2.8)–(2.9) in mixed weak form (see, e.g., [9, Chap. 6]): find $(\mathbf{u}, p, \mathbf{f}) \in \mathbf{V} \times \mathcal{P} \times \mathcal{F}$ such that

$$(3.29) \quad a(\mathbf{u}, \mathbf{v}) - b(\mathbf{v}, p) - b(\mathbf{u}, q) - \langle \mathbf{f}, \mathbf{v} \rangle_{\Gamma} + \langle \mathbf{g}, u^s \boldsymbol{\tau} + U \mathbf{e}_z \rangle_{\Gamma} - \langle \mathbf{g}, \mathbf{u} \rangle_{\Gamma} = 0 \\ \forall (\mathbf{v}, q, \mathbf{g}) \in \mathbf{V} \times \mathcal{P} \times \mathcal{F},$$

where the bilinear forms a and b are defined (using (2.10) for a) by

$$a(\mathbf{u}, \mathbf{v}) = \int_{\Omega} 2\mu(\mathbf{D}[\mathbf{u}] : \mathbf{D}[\mathbf{v}]) dV, \quad b(\mathbf{v}, q) = \int_{\Omega} q(\nabla \cdot \mathbf{v}) dV.$$

The weak problem (3.29) is well-posed if $\mathcal{F} = H^{-1/2}(\Gamma; \mathbb{R}^3)$, $\mathcal{P} = L^2(\Omega)$, and \mathbf{V} is a weighted version of $H^1(\Omega; \mathbb{R}^3)$. Supplementing problem (3.29) with the no-net-force condition (2.11) determines U given u^s . The unknown \mathbf{f} , acting as the Lagrange multiplier associated with the Dirichlet BC, is in fact the force density on Γ given by $\mathbf{f} = \boldsymbol{\sigma}[\mathbf{u}, p] \cdot \mathbf{n}$, where $\boldsymbol{\sigma}[\mathbf{u}, p] = -p\mathbf{I} + 2\mu\mathbf{D}[\mathbf{u}]$ is the stress tensor. Similarly, the adjoint problem (2.12) in weak form is as follows: find $(\hat{\mathbf{u}}, \hat{p}, \hat{\mathbf{f}}) \in \mathbf{V} \times \mathcal{P} \times \mathcal{F}$ such that

$$(3.30) \quad a(\hat{\mathbf{u}}, \mathbf{v}) - b(\mathbf{v}, \hat{p}) - b(\hat{\mathbf{u}}, q) - \langle \hat{\mathbf{f}}, \mathbf{v} \rangle_{\Gamma} + \langle \mathbf{g}, \mathbf{e}_z \rangle_{\Gamma} - \langle \mathbf{g}, \hat{\mathbf{u}} \rangle_{\Gamma} = 0 \\ \forall (\mathbf{v}, q, \mathbf{g}) \in \mathbf{V} \times \mathcal{P} \times \mathcal{F}.$$

2. *Weak formulation for material derivatives of the forward solution.* The governing weak formulation for the shape derivative $(\dot{\mathbf{u}}, \dot{\mathbf{f}}, \dot{p}, \dot{U})$ of the solution $(\mathbf{u}, \mathbf{f}, p, U)$ of the forward problem (3.29)–(2.11) is

$$(3.31) \quad a(\dot{\mathbf{u}}, \mathbf{v}) - b(\mathbf{v}, \dot{p}) - b(\dot{\mathbf{u}}, q) - \langle \dot{\mathbf{f}}, \mathbf{v} \rangle_{\Gamma} + \langle u^s \dot{\boldsymbol{\tau}}, \mathbf{g} \rangle_{\Gamma} + \langle \mathbf{e}_z, \mathbf{g} \rangle_{\Gamma} \dot{U} - \langle \dot{\mathbf{u}}, \mathbf{g} \rangle_{\Gamma} \\ = -\langle \mathbf{E}((\mathbf{u}, p), (\mathbf{v}, q)), \nabla^T \boldsymbol{\theta} \rangle_{\Omega} + \langle \mathbf{f}, \mathbf{v} \operatorname{div}_s \boldsymbol{\theta} \rangle_{\Gamma} \quad \forall (\mathbf{v}, q, \mathbf{g}) \in \mathbf{V} \times \mathcal{P} \times \mathcal{F},$$

with the symmetric in $((\mathbf{u}, p), (\mathbf{v}, q))$ tensor-valued function \mathbf{E} defined by

$$(3.32) \quad \mathbf{E}((\mathbf{u}, p), (\mathbf{v}, q)) \\ = (2\mu\mathbf{D}[\mathbf{u}] : \mathbf{D}[\mathbf{v}] - p(\nabla \cdot \mathbf{v}) - q(\nabla \cdot \mathbf{u})) \mathbf{I} - \boldsymbol{\sigma}[\mathbf{u}, p] \cdot \nabla \mathbf{v} - \boldsymbol{\sigma}[\mathbf{v}, q] \cdot \nabla \mathbf{u}.$$

The value of \dot{U} is determined by the material derivative of the no-net-force condition (2.11), which reads as

$$(3.33) \quad \langle \dot{\mathbf{f}}, \mathbf{e}_z \rangle_{\Gamma} + \langle \mathbf{f} \operatorname{div}_s \boldsymbol{\theta}, \mathbf{e}_z \rangle_{\Gamma} = 0.$$

The weak formulation (3.31) is obtained by applying the material differentiation identities (3.18), with the aid of formulas (3.17), to the variational equation (3.29), assuming the test functions in (3.29) to verify $\dot{\mathbf{v}} = \mathbf{0}$, $\dot{\mathbf{g}} = \mathbf{0}$ and $\dot{q} = 0$, i.e., to be convected under the shape perturbation (which the absence of boundary constraints in \mathcal{V} allows). The Dirichlet BC (2.9) then allows us to cancel some terms in the resulting equality.

3. Material derivatives of energy functionals and drag force. We subtract (3.31) with $(\mathbf{v}, q, \mathbf{g}) = (\mathbf{u}, p, \mathbf{f})$ from (3.29) with $(\mathbf{v}, q, \mathbf{g}) = (\dot{\mathbf{u}}, \dot{p}, \dot{\mathbf{f}})$ and use the no-net-force condition (2.11) to obtain

$$(3.34) \quad \begin{aligned} & \langle u^s \dot{\boldsymbol{\tau}}, \mathbf{f} \rangle_{\Gamma} - \langle \dot{\mathbf{f}}, u^s \boldsymbol{\tau} \rangle_{\Gamma} - \langle \dot{\mathbf{f}}, \mathbf{e}_z \rangle_{\Gamma} U \\ &= -\langle \mathbf{E}((\mathbf{u}, p), (\mathbf{u}, p)), \nabla^T \boldsymbol{\theta} \rangle_{\Omega} + \langle \mathbf{f}, (u^s \boldsymbol{\tau} + U \mathbf{e}_z) \operatorname{div}_s \boldsymbol{\theta} \rangle_{\Gamma}. \end{aligned}$$

We then use (3.34) in (3.21), which allows us to eliminate the contribution of $\dot{\mathbf{f}}$ and yields

$$(3.35) \quad J'_W(\Gamma; \boldsymbol{\theta}) = 2\langle \mathbf{f}, u^s \dot{\boldsymbol{\tau}} \rangle_{\Gamma} + \langle \mathbf{E}((\mathbf{u}, p), (\mathbf{u}, p)), \nabla^T \boldsymbol{\theta} \rangle_{\Omega}.$$

Equality (3.34) is also valid for the case where $\mathbf{u}^D = \mathbf{e}_z$, i.e., $U = 1, u^s = 0$ corresponding to the adjoint problem, since it does not rely on the no-net-force condition. Using this version in (3.22) readily yields

$$(3.36) \quad F'_0(\Gamma; \boldsymbol{\theta}) = \langle \mathbf{E}((\hat{\mathbf{u}}, \hat{p}), (\hat{\mathbf{u}}, \hat{p})), \nabla^T \boldsymbol{\theta} \rangle_{\Omega}.$$

Last (and similarly), setting $(\mathbf{v}, q, \mathbf{g}) = (\dot{\mathbf{u}}, \dot{p}, \dot{\mathbf{f}})$ in the adjoint problem (3.30) and $(\mathbf{v}, q, \mathbf{g}) = (\hat{\mathbf{u}}, \hat{p}, \hat{\mathbf{f}})$ in (3.31) of the derivative problem, then evaluating the combination (3.31)–(3.30) and using (3.33) provides

$$(3.37) \quad F_0 U'(\Gamma; \boldsymbol{\theta}) + \langle \hat{\mathbf{f}}, u^s \dot{\boldsymbol{\tau}} \rangle_{\Gamma} = -\langle \mathbf{E}((\mathbf{u}, p), (\hat{\mathbf{u}}, \hat{p})), \nabla^T \boldsymbol{\theta} \rangle_{\Omega}.$$

The functional derivatives given by (3.35)–(3.37) are thus free of any solution material derivatives.

4. Material derivatives of functionals: boundary-only form. The domain integrals involving \mathbf{E} are, in all three cases (3.35)–(3.37), recast as follows in terms of only boundary integrals:

$$(3.38)$$

- (a) $J'_W(\Gamma; \boldsymbol{\theta}) = \int_{\Gamma} [2\mu \mathbf{D}[\mathbf{u}] : \mathbf{D}[\mathbf{u}] \theta_n + 2\mathbf{f} \cdot (\dot{\mathbf{u}}^s - \nabla \mathbf{u} \cdot \boldsymbol{\theta})] dS,$
- (b) $F'_0(\Gamma; \boldsymbol{\theta}) = \int_{\Gamma} [2\mu \mathbf{D}[\hat{\mathbf{u}}] : \mathbf{D}[\hat{\mathbf{u}}] \theta_n - 2\hat{\mathbf{f}} \cdot \nabla \hat{\mathbf{u}} \cdot \boldsymbol{\theta}] dS,$
- (c) $F_0 U'(\Gamma; \boldsymbol{\theta}) = - \int_{\Gamma} [2\mu \mathbf{D}[\mathbf{u}] : \mathbf{D}[\hat{\mathbf{u}}] \theta_n - \mathbf{f} \cdot \nabla \hat{\mathbf{u}} \cdot \boldsymbol{\theta} + \hat{\mathbf{f}} \cdot (\dot{\mathbf{u}}^s - \nabla \mathbf{u} \cdot \boldsymbol{\theta})] dS.$

The proofs of formulas (3.38)(a)–(c) rests on the following identity, established in Appendix B.

LEMMA 3.6. Let (\mathbf{u}, p) and (\mathbf{v}, q) both satisfy (2.8). Then, for any vector field $\boldsymbol{\theta} \in C_0^{1,\infty}(\Omega)$, we have

$$\langle \mathbf{E}((\mathbf{u}, p), (\hat{\mathbf{u}}, \hat{p})), \nabla^T \boldsymbol{\theta} \rangle_{\Omega} = \int_{\Gamma} \mathbf{n} \cdot \mathbf{E}((\mathbf{u}, p), (\hat{\mathbf{u}}, \hat{p})) \cdot \boldsymbol{\theta} \, dS.$$

Formulas (3.38)(a)–(c) are then found by applying Lemma 3.6 to the right-hand sides of (3.35), (3.36), and (3.37) and using the definition (3.32) of \mathbf{E} , with $(\mathbf{v}, q) = (\mathbf{u}, p)$ for (3.38)(a), $(\mathbf{u}, p) = (\mathbf{v}, q) = (\hat{\mathbf{u}}, \hat{p})$ for (3.38)(b), and $(\mathbf{v}, q) = (\hat{\mathbf{u}}, \hat{p})$ for (3.38)(c).

5. Express velocity normal derivatives using traction vectors. The shape sensitivity formulas (3.38) remain somewhat inconvenient, as they involve complete velocity gradients on Γ . This can be remedied by using the decomposition $\nabla \mathbf{u} = \nabla_s \mathbf{u} + \partial_n \mathbf{u} \otimes \mathbf{n}$ of the velocity gradient (where $\nabla_s \mathbf{u}$ and $\partial_n \mathbf{u}$ respectively denote the tangential gradient and the normal derivative of \mathbf{u}) and expressing $\partial_n \mathbf{u}$ in terms of \mathbf{f} . In view of the specific form $\mathbf{u}^D = U \mathbf{e}_z + u^s \boldsymbol{\tau}$ of the Dirichlet data on Γ , this step is carried out explicitly using curvilinear coordinates, and the following expressions are found by means of straightforward algebra (see the proof given in Appendix C) for the gradient and the strain rate tensor of the forward and adjoint solutions.

LEMMA 3.7. Let $(\mathbf{u}, p, \mathbf{f})$ be the solution to the forward problem. On Γ ,

$$(3.39) \quad \begin{aligned} \nabla \mathbf{u} &= \frac{1}{2\mu} (f_n + p) (\mathbf{n} \otimes \mathbf{n} - \boldsymbol{\tau} \otimes \boldsymbol{\tau}) + \frac{R' u^s}{R\alpha} (\boldsymbol{\nu} \otimes \boldsymbol{\nu} - \boldsymbol{\tau} \otimes \boldsymbol{\tau}) \\ &\quad + \kappa u^s (\mathbf{n} \otimes \boldsymbol{\tau} - \boldsymbol{\tau} \otimes \mathbf{n}) + \frac{1}{\mu} f_{\tau} \boldsymbol{\tau} \otimes \mathbf{n}, \\ 2\mu \mathbf{D}[\mathbf{u}] &= (f_n + p) (\mathbf{n} \otimes \mathbf{n} - \boldsymbol{\tau} \otimes \boldsymbol{\tau}) + \frac{2\mu R' u^s}{R\alpha} (\boldsymbol{\nu} \otimes \boldsymbol{\nu} - \boldsymbol{\tau} \otimes \boldsymbol{\tau}) \\ &\quad + f_{\tau} (\mathbf{n} \otimes \boldsymbol{\tau} + \boldsymbol{\tau} \otimes \mathbf{n}). \end{aligned}$$

Similarly, for the solution $(\hat{\mathbf{u}}, \hat{p}, \hat{\mathbf{f}})$ of the adjoint problem, we have

$$\nabla \hat{\mathbf{u}} = \frac{1}{\mu} \hat{f}_{\tau} \boldsymbol{\tau} \otimes \mathbf{n}, \quad 2\mu \mathbf{D}[\hat{\mathbf{u}}] = \hat{f}_{\tau} (\mathbf{n} \otimes \boldsymbol{\tau} + \boldsymbol{\tau} \otimes \mathbf{n}).$$

In addition, as shown in Appendix B, the material derivative $\dot{\boldsymbol{\tau}}$ of the unit tangent to generating arcs is given by

$$(3.40) \quad \dot{\boldsymbol{\tau}} = \left(\frac{1}{\alpha} \theta'_n + \kappa \theta_{\tau} \right) \mathbf{n}.$$

The shape sensitivity formulas (3.23) to (3.25) are finally obtained by deriving explicit expressions of the right-hand sides of (3.38). First, to establish (3.23) for $J'_w(\Gamma; \boldsymbol{\theta})$, we derive the expressions

$$\begin{aligned} \mathbf{f} \cdot \dot{\mathbf{u}}^s &= u^s f_n \left(\kappa \theta_{\tau} + \frac{1}{\alpha} \theta'_n \right), \\ \mathbf{f} \cdot \nabla \mathbf{u} \cdot \boldsymbol{\theta} &= \left(\frac{1}{\mu} f_{\tau}^2 + \frac{1}{2\mu} (f_n + p) f_n - \kappa u^s f_{\tau} \right) \theta_n + \left(\frac{1}{\alpha} (u^s)' f_{\tau} + \kappa u^s f_n \right) \theta_{\tau}, \\ 2\mu \mathbf{D}[\mathbf{u}] : \mathbf{D}[\mathbf{u}] \theta_n &= \left[\frac{1}{\mu} f_{\tau}^2 + 4\mu \left(\frac{R' u^s}{R\alpha} \right)^2 + \frac{1}{\mu} (f_n + p)^2 \right] \theta_n \end{aligned}$$

with the help of (3.40) and (3.39). After rearrangement, we obtain

$$(3.41) \quad \begin{aligned} & 2\mu \mathbf{D}[\mathbf{u}] : \mathbf{D}[\mathbf{u}] \theta_n + 2\mathbf{f} \cdot (\dot{\mathbf{u}}^s - \nabla \mathbf{u} \cdot \boldsymbol{\theta}) \\ &= \left[-\frac{1}{\mu} f_\tau^2 + 4\mu \left(\frac{R' u^s}{Ra} \right)^2 + \frac{1}{\mu} (f_n + p)p + 2\kappa u^s f_\tau \right] \theta_n - \frac{2}{\alpha} f_\tau \theta_\tau (u^s)' + \frac{2}{\alpha} u^s f_n \theta_n'. \end{aligned}$$

We then similarly derive the formulas

$$(3.42) \quad \begin{aligned} & 2\mu \mathbf{D}[\hat{\mathbf{u}}] : \mathbf{D}[\hat{\mathbf{u}}] \theta_n + \hat{\mathbf{f}} \cdot (\dot{\mathbf{u}}^s - \nabla \mathbf{u} \cdot \boldsymbol{\theta}) - \mathbf{f} \cdot \nabla \hat{\mathbf{u}} \cdot \boldsymbol{\theta} \\ &= \left[\kappa u^s \hat{f}_\tau - \frac{1}{\mu} f_\tau \hat{f}_\tau + \frac{1}{2\mu} (f_n + p)\hat{p} \right] \theta_n - \frac{1}{\alpha} \hat{f}_\tau \theta_\tau (u^s)' - \frac{1}{\alpha} u^s \hat{p} \theta_n', \end{aligned}$$

$$(3.43) \quad 2\mu \mathbf{D}[\hat{\mathbf{u}}] : \mathbf{D}[\hat{\mathbf{u}}] \theta_n - 2\hat{\mathbf{f}} \cdot \nabla \hat{\mathbf{u}} \cdot \boldsymbol{\theta} = -\frac{1}{\mu} \hat{f}_\tau^2 \theta_n,$$

having in particular used that $\hat{f}_n = -\hat{p}$. The sought material derivative formulas (3.23) to (3.25) finally follow by using identities (3.41), (3.42) and (3.43) in formulas (3.38)(a)–(c).

6. *End of proof.* Steps 1 to 5 above complete the proof of identities (3.23) to (3.25), and formula (3.26) follows directly from the definition of J_{drag} given after (3.10).

4. Numerical method. In this section, we describe the main numerical methods employed for solving the shape optimization problem, utilizing the shape sensitivity formulas derived in the preceding sections.

4.1. Stokes PDE solver. The shape optimization problem requires solution of three different boundary value problems: (i) the *forward problem* with given slip velocity (2.8)–(2.11), (ii) the *adjoint problem* with given Dirichlet conditions (2.12), and (iii) the *auxiliary problem* with mixed boundary conditions (3.12) for determining the optimal slip for a given shape. Similar to our previous works [13, 12], which studied the optimization of slip velocity profiles and ciliary locomotion for a given shape Γ , we employ an indirect boundary integral equation (BIE) formulation for solving these three problems.

Specifically, we start from the single-layer potential *ansatz*, which expresses the velocity \mathbf{u} as a convolution of an unknown axially symmetric density function ζ defined on Γ with the Green's function for the Stokes equations:

$$(4.1) \quad \begin{aligned} \mathbf{u}(\mathbf{x}) &= \mathcal{S}[\zeta](\mathbf{x}), \\ \text{where } \mathcal{S}[\zeta](\mathbf{x}) &= \frac{1}{8\pi\mu} \int_{\Gamma} \left(\frac{1}{|\mathbf{r}|} \mathbf{I} + \frac{\mathbf{r} \otimes \mathbf{r}}{|\mathbf{r}|^3} \right) \zeta(\mathbf{y}) dS \quad \text{and} \quad \mathbf{r} = \mathbf{x} - \mathbf{y}. \end{aligned}$$

The ansatz (4.1) satisfies the Stokes PDE by construction, and taking the limit as \mathbf{x} approaches Γ from the exterior and applying boundary conditions for each of the three problems results in a set of BIEs for the unknown density ζ . The traction vector \mathbf{f} and pressure density p on the surface Γ can be evaluated as a convolution of ζ with the traction and the pressure kernels, respectively:

$$(4.2) \quad \begin{aligned} \mathbf{f}(\mathbf{x}) &= -\frac{1}{2} \zeta(\mathbf{x}) + \mathcal{K}[\zeta](\mathbf{x}), \\ \text{where } \mathcal{K}[\zeta](\mathbf{x}) &= \frac{3}{4\pi} \int_{\Gamma} \left(\frac{\mathbf{r} \otimes \mathbf{r}}{|\mathbf{r}|^5} \right) (\mathbf{r} \cdot \mathbf{n}(\mathbf{x})) \zeta(\mathbf{y}) dS, \end{aligned}$$

$$(4.3) \quad p(\mathbf{x}) = -\frac{1}{2}\zeta(\mathbf{x}) \cdot \mathbf{n}(\mathbf{x}) + \frac{1}{4\pi} \int_{\Gamma} \frac{\mathbf{r} \cdot \zeta(\mathbf{y})}{|\mathbf{r}|^3} dS.$$

In the case of the adjoint problem, denoting the unknown density by $\hat{\zeta}$, substituting the ansatz in the Dirichlet boundary condition in (2.12), and then evaluating the traction by (4.2), we get

$$(4.4) \quad \mathcal{S}[\hat{\zeta}](\mathbf{x}) = \mathbf{e}_z, \quad \hat{\mathbf{f}} = -\frac{1}{2}\hat{\zeta} + \mathcal{K}[\hat{\zeta}] \quad (\text{BIE for adjoint problem (2.12)}).$$

Then the mixed boundary conditions featured in the auxiliary problem (3.12) yield

$$(4.5) \quad \begin{aligned} \left(-\frac{1}{2} + \mathcal{K}\right)[\tilde{\zeta}] \cdot \boldsymbol{\tau} &= \hat{\mathbf{f}} \cdot \boldsymbol{\tau} && (\text{BIEs for auxiliary problem (3.12)}). \\ \mathcal{S}[\tilde{\zeta}] \cdot \mathbf{n} &= 0 \end{aligned}$$

Similarly, for the forward problem (2.9), the unknowns ζ and U can be obtained by substituting (4.1) in (2.9) and (4.2) in (2.11), yielding for any \mathbf{x} on Γ ,

$$(4.6) \quad \begin{aligned} \mathcal{S}[\zeta](\mathbf{x}) - U\mathbf{e}_z &= \mathbf{u}^s(\mathbf{x}) \\ \left\langle \left(-\frac{1}{2} + \mathcal{K}\right)[\zeta], \mathbf{e}_z \right\rangle_{\Gamma} &= 0 && (\text{BIEs for the forward problem (2.9)}). \end{aligned}$$

We convert the weakly singular boundary integrals in (4.4)–(4.6) into convolutions on the generating curve γ by performing an analytic integration in the orthoradial direction and applying a high-order quadrature rule designed to handle the log-singularity of the resulting kernels [26]. In addition, shape sensitivity formulas in Proposition 3.4 require evaluating the pressure fields p and \hat{p} on the particle surface Γ . We make use of a generalized Gaussian quadrature rule, developed in [7], for accurate numerical integration of the exhibited strong r^{-2} -singularity of the kernel in (4.3).

4.2. Finite parametrizations of slip velocity and shape. We employ fifth-order B-splines to parametrize the unknowns of the optimization problems (3.6) and (3.10), namely the scalar slip velocity profile u^s and the functions R, Z that define Γ through (2.2), by

$$(4.7) \quad u^s(t) = \xi_u^T \mathbf{w}(t), \quad R(t) = \xi_R^T \mathbf{B}(t), \quad Z(t) = \xi_Z^T \mathbf{B}(t), \quad t \in [0, \pi].$$

The vector-valued functions $\mathbf{w}(t)$ and $\mathbf{B}(t)$ are provided in Appendix A. The design vectors for u^s and γ are denoted by $\xi_u = (\xi_u^1, \dots, \xi_u^{N_u})^T$ and $\xi_{\gamma} = (\xi_R, \xi_Z) = (\xi_R^1, \dots, \xi_R^{N_R}, \xi_Z^1, \dots, \xi_Z^{N_Z})^T$, respectively. In order to satisfy the constraints (2.1)(a), (c), the shape design vector ξ_{γ} has $N_R + N_Z - 4$ degrees of freedom, as $\xi_R^1, \xi_R^{N_R}, \xi_Z^1, \xi_Z^{N_Z}$ are determined upon other entries in ξ_{γ} (see Appendix A).

Then transformation velocities θ associated with the parametrization (4.7) may be defined as

$$(4.8) \quad \theta = \xi_R^T \mathbf{B}(t) \mathbf{e}_r + \xi_Z^T \mathbf{B}(t) \mathbf{e}_z,$$

where $(\zeta_R, \zeta_Z) =: \zeta_{\gamma}$ define perturbation directions for the shape parameter vectors ξ_R, ξ_Z , which must be consistent with (2.1)(a), (c) and are otherwise arbitrary.

4.3. Numerical optimization scheme. We use the augmented Lagrangian method (ALM) to adapt the constrained optimization problem (3.6) to a sequence of unconstrained problems [23, Chap. 17] of the form

(4.9)

$$\min_{\Gamma} \mathcal{L}_A(\Gamma) \quad \text{with} \quad \mathcal{L}_A(\Gamma) = -E(z^s, \Gamma) - \lambda_l C_\nu(\Gamma) + \frac{\sigma_l}{2} C_\nu^2(\Gamma), \quad l = 0, 1, 2, \dots,$$

where $z^s = z^s[\Gamma]$ is the slip velocity yielding optimal efficiency for a given shape Γ , given by Proposition 3.1. The variable λ_l is an explicit estimate of the Lagrange multiplier, and σ_l is a penalty parameter. The optimization algorithm fixes the values of λ_l and σ_l at the l th iteration and performs minimization for \mathcal{L}_A . Figure 4.1

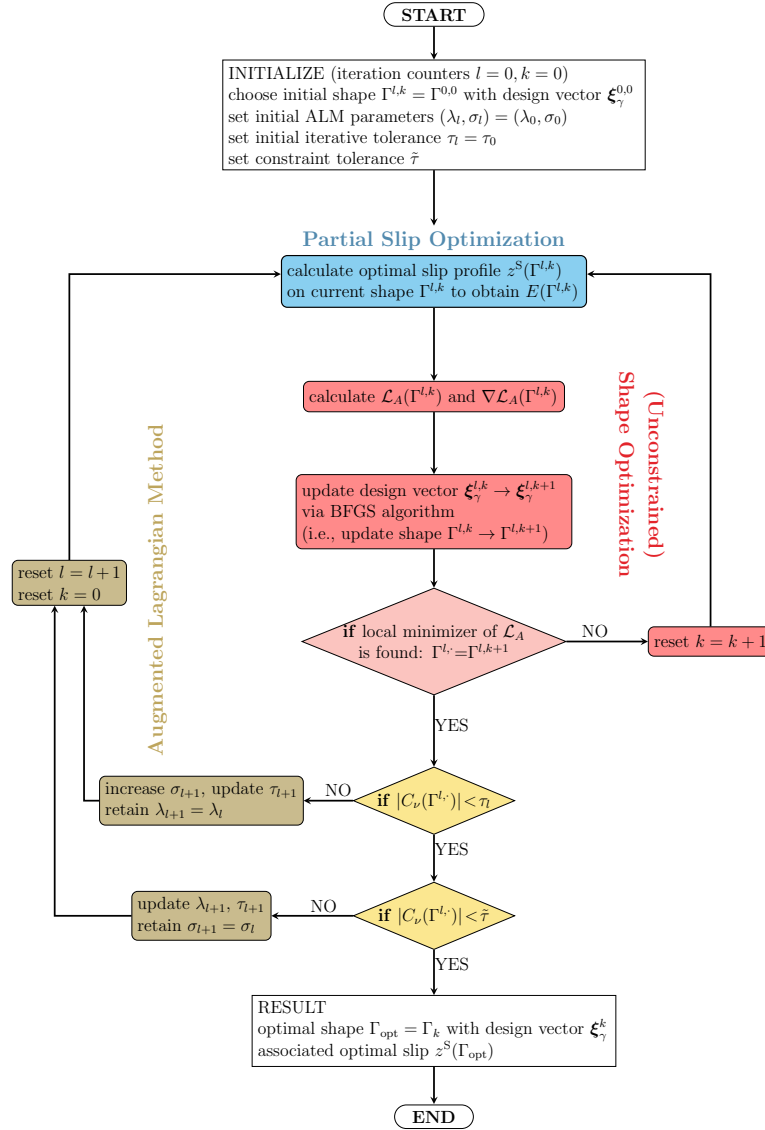


FIG. 4.1. Framework of the optimization algorithm for the maximum swimming efficiency. The algorithm consists of three main parts shown in different colors. The single block in blue is the slip optimization as described in section 3.2. It is worth noting that the slip optimization process is nested in the shape optimization process (in red/pink). The process in yellow/brown color briefly demonstrates the algorithm of the augmented Lagrangian method (ALM) in section 4.3.

depicts the framework of the optimization method with the slip optimization step implemented internally. In this flowchart, the shape Γ and its design vector ξ_γ are often accompanied by superscripts l, k . The first number l indicates the iteration of ALM when updating λ_l , σ_l , and the second number indicates the iteration in the unconstrained shape optimization problem (4.9) with specific l . The optimization process starts with an arbitrary initial shape $\Gamma^{0,0}$ given by the design vector $\xi_\gamma^{0,0}$. The optimal slip profile for the current shape is calculated directly as described in section 3.2, shown as a single blue block in Figure 4.1. The shape is then updated via the BFGS algorithm for the unconstrained problem (4.9), which makes use of the shape derivative of $E(\Gamma)$ given by Proposition 3.5, and the slip profile must be recalculated in every iteration of the BFGS algorithm. When the optimal shape is found, the process moves to parameter updating of ALM (if tolerance criteria are not satisfied); then a new unconstrained problem (4.9) is defined and implemented. If the local minimizer of (4.9) for current l satisfies the tolerance criteria, the optimization is completed and outputs the optimal shape.

Similarly, the constrained drag force minimization problem (3.10) is solved using the sequence of unconstrained problems

$$(4.10) \quad \min_{\Gamma} \mathcal{L}_A(\Gamma) \quad \text{with} \quad \mathcal{L}_A(\Gamma) = J_{\text{drag}} - \lambda_l C_\nu + \frac{\sigma_l}{2} C_\nu^2, \quad l = 0, 1, 2, \dots$$

The optimization is implemented similarly as Figure 4.1, except that the partial slip optimization step is omitted. Solving the unconstrained problem (4.10) makes use of (3.26) for the shape derivative of the drag force. It does not involve any slip velocity, and thus the optimization starts with calculating \mathcal{L}_A and $\nabla \mathcal{L}_A$ in (4.10) directly. The rest of the process remains the same as before.

5. Results and discussion. In this section, we first validate the shape sensitivity formulas derived in section 3.4, referring the reader to [13] for the validation of the forward solver. Then we present several numerical experiments to demonstrate the shape optimization approach for microswimmers and analyze the optimal shapes obtained for various reduced volumes. Additionally, we compare the results with those of the drag minimization problem to highlight the differences arising from the differing objectives of maximizing efficiency or minimizing drag.

5.1. Verification of shape sensitivities. Here we validate the shape sensitivity formulas (3.26) and (3.28) by comparing them with the numerical approximations via the finite-difference method. We use the central difference formula for comparison, given by

$$(5.1) \quad J'_{\text{FD}} = \frac{J(\Gamma(\xi_\gamma + \eta \zeta_\gamma)) - J(\Gamma(\xi_\gamma - \eta \zeta_\gamma))}{2\eta},$$

where J is either $E(\Gamma)$ or $J_{\text{drag}}(\Gamma)$ and ζ_γ is a shape parameter perturbation direction that defines a transformation velocity θ through (4.8).

We choose an arbitrary initial shape and then perturb it into a variety of other arbitrary shapes. Table 5.1 lists the absolute and relative errors between the analytic formula evaluations and their finite-difference approximations, with the step size $\eta = 10^{-3}$ in (5.1) for all cases. The error results validate the correctness of the analytic shape sensitivity formulas given in section 3.4.

5.2. Optimization results. First, we showcase the iterative shape optimization process towards a maximal efficiency shape in Figure 5.1, starting from an arbitrary

TABLE 5.1

Comparison of shape sensitivities obtained by analytic formulas and by the central finite-difference scheme. The absolute errors (abs.err.) is $|J' - J'_{FD}|$, where J' is the result of the analytic sensitivity formula, J'_{drag} in (3.26) or E' in (3.28), and J'_{FD} is the result of (5.1). The relative error (rel.err.) is calculated by $|(J' - J'_{FD})/J'_{FD}|$. Note that the perturbed shapes are shown at $\eta = 1$ for visualization purposes to highlight the direction of perturbation.

Initial Γ	Perturbed Γ	J'_{drag} abs.err.	J'_{drag} rel.err.	E' abs.err.	E' rel.err.
		4.96×10^{-8}	4.76×10^{-7}	2.60×10^{-7}	5.55×10^{-7}
		2.89×10^{-9}	1.14×10^{-7}	6.98×10^{-8}	5.60×10^{-7}
		2.73×10^{-7}	1.12×10^{-6}	7.33×10^{-7}	7.32×10^{-7}

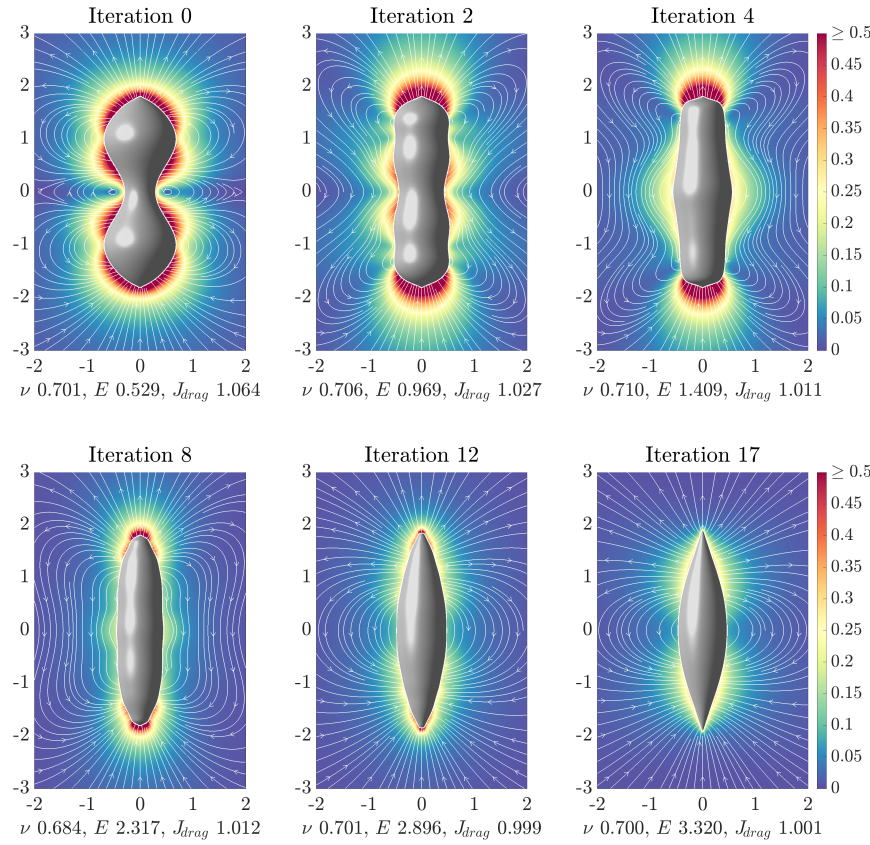


FIG. 5.1. Snapshots from the shape optimization of an initially peanut-shaped microswimmer with reduced volume, $\nu_0 = 0.7$. Here the fluid velocity is shown in the lab (fixed) frame and the propulsion velocity U is scaled to one.

peanut-like shape. The flow field snapshots around the microswimmer driven by the optimal slip profile that maximizes the swimming efficiency are demonstrated during the optimization process. In particular, a peanut-shaped microswimmer with $\nu \approx 0.7$ is used as the initial shape. The high-velocity region can be observed around the entire swimmer in early iterations. This high-velocity region, in turn, leads to a low swimming efficiency at $E = 53\%$. During the optimization process, the swimmer first transitions from its original concave shape to a convex shape that resembles a prolate spheroidal shape with blunt poles (iteration 12), and then “sharpens” the poles in the next few iterations (iteration 17), leading to a swimming efficiency as high as $E = 332\%$. We note that the high-velocity region is gradually reduced during the optimization, and the reduction progresses from the equatorial region toward the poles. The final shape has sharp-looking poles, which, however, are smooth (albeit of high curvature) and so is the optimal slip profile z^s . Using numerical experiments, we verified that the converged shape and profile are stable under refinement via increasing the number of shape parameters.

Next, we consider several initial shapes whose reduced volumes are in the range $0.5 \leq \nu \leq 1.0$ and optimize their shape and associated slip profiles. The swimming efficiency corresponding to the optimal shape and slip is referred to as the maximal swimming efficiency and is shown in Figure 5.2(a) in orange stars as a function of reduced volume. Since the only possible shape for $\nu = 1$ is a sphere, the optimization problem reduces to finding the optimal slip profile of a sphere to maximize the swimming efficiency. In this case, we recover the standard result that the optimal profile is a sine function $u^s = \sin(t)$ that yields the swimming efficiency $E = 50\%$ [20]. As ν decreases, the shapes of the microswimmers deviate from a sphere. The maximal swimming efficiency monotonically increases with the decrease of ν . For all reduced volumes we test, the optimal shapes that maximize the swimming efficiency are pointy elongated front-back symmetric shapes, as shown in the insets of Figure 5.2(a). As references, we optimize the slip profiles on two other shape families

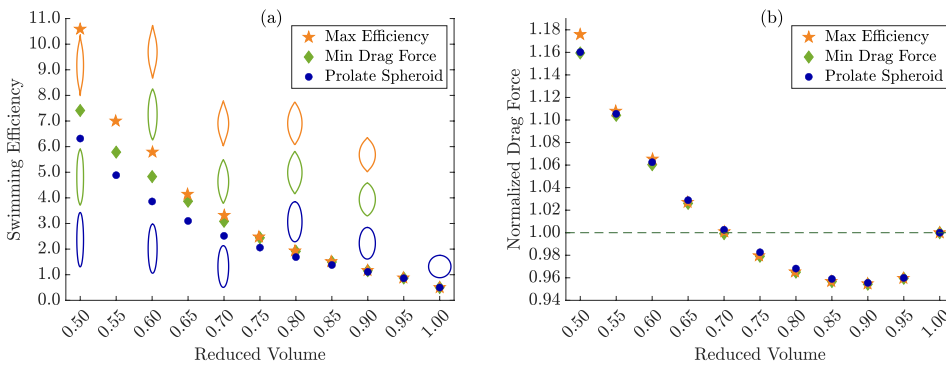


FIG. 5.2. (a) Swimming efficiency versus reduced volume of different shape families. The shapes and the slip profiles that maximize the swimming efficiencies are obtained using algorithms detailed in Figure 4.1. The swimming efficiencies for the prolate spheroid and the shape that minimizes the fluid drag are obtained by the slip optimization algorithm detailed in section 3.2, while the body shapes are fixed. For $\nu = 0.5, 0.6, 0.7, 0.8, 0.9, 1.0$, the shapes corresponding to the maximal efficiency (orange), the minimal drag force (green), and the prolate spheroid (blue) are shown vertically aligned with its reduced volume. (b) Normalized drag force versus reduced volume of different shape families. No significant difference is found in the fluid drag force between the three shape families for any given reduced volume, as long as the shape is similar to elongated front-back symmetric prolate spheroids.

and compare the swimming efficiencies against the maximal swimming efficiencies. Specifically, we consider prolate spheroids and shapes that minimize the fluid drag for given reduced volumes ν . The swimming efficiencies and the corresponding shapes are presented in Figure 5.2(a). To obtain the swimming efficiencies corresponding to these shape families, we apply the partial optimization method with fixed shape described in section 3.2. Notably, for any given reduced volume, the prolate spheroid always underperforms its two counterparts (the shape that maximizes the swimming efficiency and the shape that minimizes the drag force). The swimming efficiencies of the shapes that minimize fluid drag are no more than 10% worse than those of the optimal shapes when $0.8 \leq \nu \leq 1.0$ but become less competitive when ν is further decreased. For example, when $\nu = 0.50$, the swimming efficiencies of the prolate spheroid and the shape that minimizes fluid drag are 632% and 741%, respectively, significantly lower than 1059% obtained by the optimal shape.

Unlike the maximal swimming efficiency, the drag force required to tow a rigid body along the axis of symmetry at unit speed does not vary monotonically with the reduced volume. Figure 5.2(b) shows the drag force normalized by the force required to tow a rigid sphere of the same volume. The drag force is minimized when $\nu \approx 0.90$, in which case the normalized drag force is approximately 0.95, consistent with the classical results [25, 6]. Further decreasing the reduced volume increases the fluid drag. In fact, our results show that shapes with $\nu < 0.70$ experience higher fluid drag compared to the spheres of the same volume. That being said, unlike the drastic effect of reduced volume on the swimming efficiency, the change in the fluid drag resulting from the change in shape is rather moderate, ranging from the low of 0.95 to the high of 1.18. The values of swimming efficiencies and fluid drag for these three shape families at different reduced volumes are shown in Table 5.2.

The three microswimmers of the same reduced volume $\nu = 0.5$ are shown in Figure 5.3. The shown flow fields correspond to the optimal slip profiles for these shapes. All microswimmers are swimming at the unit translational velocity. In addition to the front-back shape symmetries, the optimal slip profiles for each of these shapes are also front-back symmetric, as expected from the linearity of Stokes equations. The fluid velocities around the microswimmers are faster closer to the swimmer's body because of the slip-boundary conditions and quickly decay to 0 away from the swimmer. Compared to the two pointy shapes, the prolate spheroid has a bigger region with high velocities close to the poles. These high-velocity regions are sources of extra power loss (fluid dissipation) that negatively impact swimming efficiencies.

In all the numerical examples presented, the generating curve γ (Figure 1.1) is divided into 60 panels, each containing 10 Gauss-Legendre quadrature points, to solve the forward problems. The whole optimization procedure outlined in Figure 5.1 took about one hour on an Apple MacBook Air equipped with an M1 chip. A MATLAB implementation is available at <https://github.com/ruowenliu/axisym3Dswimmer/>.

6. Conclusions. In this work, we proposed a computational framework that optimizes the shape and the slip velocity of a slip-driven axisymmetric microswimmer. The objective function is chosen to be the swimming efficiency in the fluid medium enclosing the microswimmer, and the microswimmers are subject to constant reduced volumes. The forward problems are solved using a boundary integral equation (BIE) method of high accuracy.

The optimization is performed iteratively, during which the optimal slip profile for a given shape and the optimal shape for a given slip profile are updated. We use an augmented Lagrangian method (ALM) to enforce the constraint of constant reduced

TABLE 5.2

Comparison of a variety of constraints and shapes. Selected corresponding shapes are exhibited in Figure 5.2. The max efficiency shapes are obtained from using the min drag force shape as the initial shape.

Reduced volume constraint	Microswimmer shape type		
	Prolate spheroid	Max efficiency	Min drag force
$\nu_0 = 0.50$	ν	0.500	0.500
	E	6.317	7.411
	J_{drag}	1.160	1.159
$\nu_0 = 0.55$	ν	0.550	0.550
	E	4.885	5.785
	J_{drag}	1.105	1.104
$\nu_0 = 0.60$	ν	0.600	0.600
	E	3.860	4.831
	J_{drag}	1.063	1.060
$\nu_0 = 0.65$	ν	0.650	0.650
	E	3.099	3.869
	J_{drag}	1.029	1.026
$\nu_0 = 0.70$	ν	0.700	0.700
	E	2.517	3.084
	J_{drag}	1.003	0.999
$\nu_0 = 0.75$	ν	0.750	0.750
	E	2.059	2.442
	J_{drag}	0.983	0.979
$\nu_0 = 0.80$	ν	0.800	0.800
	E	1.688	1.915
	J_{drag}	0.968	0.965
$\nu_0 = 0.85$	ν	0.850	0.850
	E	1.379	1.497
	J_{drag}	0.959	0.957
$\nu_0 = 0.90$	ν	0.900	0.900
	E	1.111	1.158
	J_{drag}	0.956	0.954
$\nu_0 = 0.95$	ν	0.950	0.950
	E	0.862	0.872
	J_{drag}	0.960	0.960
$\nu_0 = 1.00$	ν	1.000	1.000
	E	0.500	0.500
	J_{drag}	1.000	1.000

volume. The slip optimization is formulated as a symmetric generalized eigenvalue problem that requires only solving one forward problem with mixed boundary condition (3.12) in addition to the adjoint problem (2.12), an improvement of our previous work [13], which entailed solving one forward problem for each basis function of the slip profile. Shape sensitivity formulas tailored for the problem and suitable for direct use within the adopted BIE framework are derived in boundary-only form, with validations against finite-difference evaluations showing excellent agreement.

Our optimization results show that the optimal shape for the axisymmetric slip-driven microswimmer with a given reduced volume is a front-back symmetric elongated shape with sharp tips. Optimal slip profiles associated with these shapes result in small high-velocity regions close to the microswimmer. The hydrodynamic efficiency can be significantly higher than that of a prolate spheroid with the same

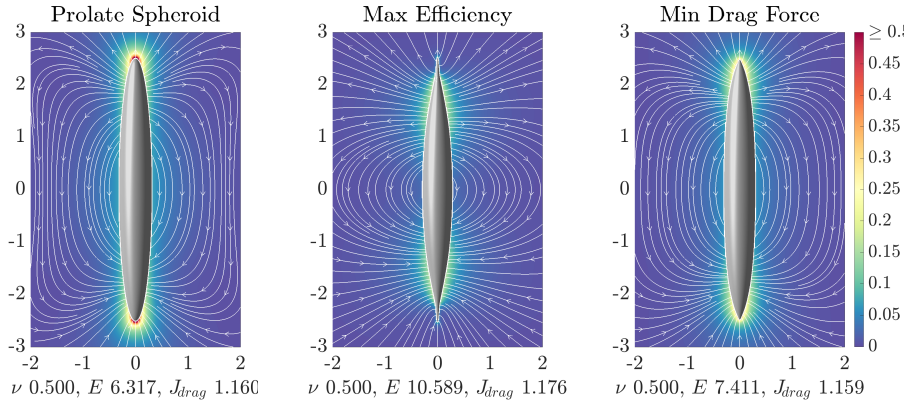


FIG. 5.3. Velocity flow fields (in lab frame) for different body shapes when the reduced volume is $\nu = 0.5$. The swimming translation velocity U is scaled to one.

reduced volume ν , especially at small ν 's. It is also worthy to note that the shape that minimizes the fluid drag also outperforms the spheroids at given ν .

We note that the optimal shapes obtained here are different than those in [27], in which the optimal shapes demonstrate ripple-like features for large minimal-curvature constraints and long protrusions from poles for small minimal-curvature constraints. In the latter case, the optimal slip velocity is high close to the tips of the protrusions and roughly uniform over the “body” of the swimmer. Our results, in contrast, indicate that the optimal swimmer shapes are more regular if we replace the minimum curvature constraint by a constant reduced volume constraint.

Appendix A. Parametrization using B-splines. We first denote the 5th-order B-spline on knots $\{0, 1, 2, 3, 4, 5, 6\}$ by $\mathcal{B}_0(t)$. By horizontal shift, let $\mathcal{B}_k(t) = \mathcal{B}_0(t - k)$ for any integer k . For the parameter domain $[0, L]$ (L being either π or 2π), the following transformation of \mathcal{B}_k is used:

$$(A.1) \quad B_k(t) = \mathcal{B}_{k-6} \left(\frac{tN_L}{L} \right), \quad k = 1, 2, \dots, (N_L + 5), \quad t \in [0, L],$$

where N_L is the number of uniform subintervals of $[0, L]$. Denote $N_\gamma = (N_L + 5)$.

The (scalar) slip velocity profile u^s is used to characterize the slip velocity \mathbf{u}^s on Γ with $t \in [0, \pi]$. We obtain N_u (uniform) interior grid points of u^s ,

$$(A.2) \quad \begin{aligned} (a) \quad & u_0 = u^s(0) = 0, \quad u_{N_u+1} = u^s(\pi) = 0, \\ (b) \quad & u_k = u^s \left(\frac{k\pi}{N_u + 1} \right), \quad k = 1, \dots, N_u, \quad \text{on } \gamma, \end{aligned}$$

where (A.2)(a) stems from (2.7). In practice, an extended vector \mathbf{v}_{ext} for $t \in [0, 2\pi]$ is used to fit B-spline interpolation,

$$\mathbf{v}_{\text{ext}} = (0, u_1, u_2, \dots, u_{N_u-1}, u_{N_u}, 0, -u_{N_u}, -u_{N_u-1}, \dots, -u_2, -u_1, 0)^T.$$

The purpose of \mathbf{v}_{ext} is to maintain periodicity of derivatives at the poles. For a given \mathbf{v}_{ext} , a function $w(t)$ is constructed by

$$(A.3) \quad w(t) = \mathbf{c}^T \mathbf{B}(t),$$

where $\mathbf{B}(t) = (B_1(t), \dots, B_{2N_u+7}(t))^T$ is defined by (A.1). The vector $\mathbf{c} = (c_1, \dots, c_{2N_u+7})^T$ is solved by

$$(A.4) \quad \begin{cases} w\left(\frac{\pi(i-1)}{N_u+1}\right) = v_i, & i = 1, \dots, 2N_u + 3, \\ \frac{d^n w(t)}{dt^n} \Big|_{t=0} = \frac{d^n w(t)}{dt^n} \Big|_{t=\pi}, & n = 1, 2, 3, 4, \end{cases}$$

where v_i is the i th component of \mathbf{v}_{ext} .

The component function $w_k(t)$ in $\mathbf{w}(t) = (w_1(t), \dots, w_{N_u}(t))^T$ in (4.7) is obtained by letting $k \in \{1, \dots, N_u\}$, $u_k = 1$, and $u_n = 0$ when $n \neq k$ and solving for \mathbf{c} in (A.3) by (A.4).

The representations of R and Z involve B_k directly, and thus we denote $\mathbf{B}(t) = (B_1(t), \dots, B_{N_\gamma}(t))^T$ in (4.7). An arbitrary $\boldsymbol{\xi}_\gamma$ does not satisfy (2.1)(a), (c); therefore, we determine the value of ξ_R^1 using $R(0) = 0$ by the values of $\xi_R^2, \xi_R^3, \xi_R^4, \xi_R^5$, considering the fact that $B_k(0) \neq 0$ only for $k \leq 5$. Choosing $N_\gamma > 10$, we similarly determine $\xi_R^{N_\gamma}$ by enforcing $R(\pi) = 0$ using the values of $\xi_R^{N_\gamma-4}, \xi_R^{N_\gamma-3}, \xi_R^{N_\gamma-2}, \xi_R^{N_\gamma-1}$. Similarly, ξ_Z^1 is determined on the values of $\xi_Z^2, \xi_Z^3, \xi_Z^4, \xi_Z^5$ by $Z'(0) = 0$ and $\xi_Z^{N_\gamma}$ on the values of $\xi_Z^{N_\gamma-4}, \xi_Z^{N_\gamma-3}, \xi_Z^{N_\gamma-2}, \xi_Z^{N_\gamma-1}$ by $Z'(\pi) = 0$. These conditions reduce the degree of freedom of $\boldsymbol{\xi}_\gamma$ from $2N_\gamma$ to $(2N_\gamma - 4)$.

Throughout all the experiments in this work, for the shape geometry R and Z , we set $L = \pi$, $N_\gamma = 21$; and for the slip profile u^s , we set $L = 2\pi$ and $N_u = 99$.

Appendix B. Auxiliary proofs.

Proof of Lemma 3.6. A straightforward derivation shows that $\nabla \cdot \mathbf{E}((\mathbf{u}, p), (\mathbf{u}, p)) = \mathbf{0}$ holds for any (\mathbf{u}, p) satisfying (2.8) (use component notation, and verify that $\sum_j \partial_j E_{ij} = 0$, $i = 1, 2, 3$). We consequently have

$$(B.1) \quad \begin{aligned} \mathbf{E}((\mathbf{u}, p), (\mathbf{u}, p)) : \nabla^T \boldsymbol{\theta} \\ = \nabla \cdot [\mathbf{E}((\mathbf{u}, p), (\mathbf{u}, p)) \cdot \boldsymbol{\theta}] - [\nabla \cdot \mathbf{E}((\mathbf{u}, p), (\mathbf{u}, p))] \cdot \boldsymbol{\theta} = \nabla \cdot [\mathbf{E}((\mathbf{u}, p), (\mathbf{u}, p)) \cdot \boldsymbol{\theta}]. \end{aligned}$$

Then, observing that $((\mathbf{u}, p), (\mathbf{v}, q)) \mapsto \mathbf{E}((\mathbf{u}, p), (\mathbf{v}, q))$ defines a symmetric bilinear form, we invoke the polarization identity and obtain

$$\begin{aligned} 4\mathbf{E}((\mathbf{u}, p), (\hat{\mathbf{u}}, \hat{p})) : \nabla^T \boldsymbol{\theta} \\ = [\mathbf{E}((\mathbf{u} + \hat{\mathbf{u}}, p + \hat{p}), (\mathbf{u} + \hat{\mathbf{u}}, p + \hat{p})) - \mathbf{E}((\mathbf{u} - \hat{\mathbf{u}}, p - \hat{p}), (\mathbf{u} - \hat{\mathbf{u}}, p - \hat{p}))] : \nabla^T \boldsymbol{\theta} \\ = \nabla \cdot [\mathbf{E}((\mathbf{u} + \hat{\mathbf{u}}, p + \hat{p}), (\mathbf{u} + \hat{\mathbf{u}}, p + \hat{p})) \cdot \boldsymbol{\theta} - \mathbf{E}((\mathbf{u} - \hat{\mathbf{u}}, p - \hat{p}), (\mathbf{u} - \hat{\mathbf{u}}, p - \hat{p})) \cdot \boldsymbol{\theta}] \\ = 4\nabla \cdot [\mathbf{E}((\mathbf{u}, p), (\hat{\mathbf{u}}, \hat{p})) \cdot \boldsymbol{\theta}], \end{aligned}$$

whereupon applying the first Green identity (divergence theorem) completes the proof of the claimed identity. \square

Proof of formula (3.40). Let the parametric representation of $\Gamma_\eta(\boldsymbol{\theta})$ be of the form (3.15). We seek the derivative of the unit tangent vector on Γ_η , given by

$$(B.2) \quad \alpha_\eta(t, \phi) \boldsymbol{\tau}_\eta(t, \phi) = \partial_s \mathbf{x}_\eta(t, \phi)$$

with respect to η and at $\eta = 0$. Since $\boldsymbol{\theta} = \partial_\eta \mathbf{x}_\eta(t, \phi)$, we have

$$(B.3) \quad \partial_\eta \alpha_\eta(t, \phi) \Big|_{\eta=0} = \frac{\partial_t \mathbf{x}_\eta(t, \phi) \cdot \partial_{\eta s} \mathbf{x}_\eta(t, \phi)}{\alpha_\eta(t, \phi)} \Big|_{\eta=0} = [\boldsymbol{\tau} \cdot \partial_s \boldsymbol{\theta}](t, \phi).$$

The derivative $\dot{\boldsymbol{\tau}} := \partial_\eta \boldsymbol{\tau}|_{\eta=0}$ is hence evaluated from (B.2), (B.3), and (2.5) as

$$(B.4) \quad \begin{aligned} \dot{\boldsymbol{\tau}}(t, \phi) &= \partial_\eta \boldsymbol{\tau}_\eta(t, \phi) \Big|_{\eta=0} = \frac{1}{\alpha(t)} (\partial_t \boldsymbol{\theta} - [\boldsymbol{\tau} \cdot \partial_s \boldsymbol{\theta}] \boldsymbol{\tau})(t, \phi) \\ &= \frac{1}{\alpha(t)} ([\mathbf{n} \cdot \partial_s \boldsymbol{\theta}] \mathbf{n})(t, \phi) = \left[\kappa \theta_\tau + \frac{1}{\alpha} \theta'_n \right] (t) \mathbf{n}(t, \phi), \end{aligned}$$

which completes the proof of (3.40). \square

Appendix C. Differential operators using curvilinear coordinates and proof of Lemma 3.7. Let points \mathbf{x} in a tubular neighborhood V of Γ be given in terms of curvilinear coordinates (t, h) , so that

$$\mathbf{x} = \mathbf{x}(t, \phi) + h \mathbf{n}(t, \phi),$$

with $\mathbf{x}(t, \phi)$ and $\mathbf{n}(t, \phi)$ as given in (2.2) and (2.3), respectively, and let

$$(C.1) \quad \mathbf{v}(\mathbf{x}) = v_\tau(t, h) \boldsymbol{\tau}(t, \phi) + v_n(t, h) \mathbf{n}(t, \phi)$$

denote a generic axisymmetric vector field in V . Then, at any point $\mathbf{x} = \mathbf{x}(t, \phi)$ on Γ (i.e., at $h = 0$), we have

$$\begin{aligned} \nabla \mathbf{v} &= \left(\frac{1}{\alpha} \partial_t v_s - \kappa v_n \right) \boldsymbol{\tau} \otimes \boldsymbol{\tau} + \left(\frac{1}{\alpha} \partial_t v_n + \kappa v_\tau \right) \mathbf{n} \otimes \boldsymbol{\tau} \\ &\quad + \frac{1}{\alpha R} (R' v_\tau + Z' v_n) \boldsymbol{\nu} \otimes \boldsymbol{\nu} + \partial_h v_\tau \boldsymbol{\tau} \otimes \mathbf{n} + \partial_h v_n \mathbf{n} \otimes \mathbf{n}, \\ \nabla \cdot \mathbf{v} &= \frac{1}{\alpha} \partial_t v_\tau - \kappa v_n + \frac{1}{\alpha R} (R' v_\tau + Z' v_n) + \partial_h v_n, \end{aligned}$$

where $\boldsymbol{\nu} = \sin \phi \mathbf{e}_x - \cos \phi \mathbf{e}_y = \mathbf{n} \times \boldsymbol{\tau}$. In particular, the transformation velocity $\boldsymbol{\theta}$ being of the form (C.1), we have

$$(C.2) \quad \operatorname{div}_s \boldsymbol{\theta} = \frac{1}{R\alpha} [\partial_t (R\theta_\tau) + (Z' - \kappa R)\theta_n].$$

Assuming incompressibility, the condition $\nabla \cdot \mathbf{v} = 0$ can be used for eliminating $\partial_h v_n$ and we obtain

$$(C.3) \quad \begin{aligned} \nabla \mathbf{v} &= \left(\frac{1}{\alpha} \partial_t v_s - \kappa v_n \right) (\boldsymbol{\tau} \otimes \boldsymbol{\tau} - \mathbf{n} \otimes \mathbf{n}) + \left(\frac{1}{\alpha} \partial_t v_n + \kappa v_\tau \right) \mathbf{n} \otimes \boldsymbol{\tau} + \partial_h v_\tau \boldsymbol{\tau} \otimes \mathbf{n} \\ &\quad + \frac{1}{\alpha R} (R' v_\tau + Z' v_n) (\boldsymbol{\nu} \otimes \boldsymbol{\nu} - \mathbf{n} \otimes \mathbf{n}). \end{aligned}$$

For the forward solution, we have $\mathbf{u} = U \mathbf{e}_z + u^s \boldsymbol{\tau} = (u^s + \frac{1}{\alpha} U Z') \boldsymbol{\tau} - \frac{1}{\alpha} U R' \mathbf{n}$ on Γ . Recalling that $2\mathbf{D}[\mathbf{u}] = \nabla \mathbf{u} + \nabla^\top \mathbf{u}$ and using $\kappa = \frac{1}{\alpha^3} (Z' R'' - R' Z'')$ and $R'^2 + Z'^2 = \alpha^2$, we obtain

$$(C.4) \quad \begin{aligned} \nabla \mathbf{u} &= \frac{(u^s)'}{\alpha} \boldsymbol{\tau} \otimes \boldsymbol{\tau} + \frac{R' u^s}{R\alpha} \boldsymbol{\nu} \otimes \boldsymbol{\nu} - \frac{(R u^s)'}{R\alpha} \mathbf{n} \otimes \mathbf{n} + \kappa u^s \mathbf{n} \otimes \boldsymbol{\tau} + \partial_h u_\tau \boldsymbol{\tau} \otimes \mathbf{n} \\ &= \frac{(R u^s)'}{R\alpha} (\boldsymbol{\tau} \otimes \boldsymbol{\tau} - \mathbf{n} \otimes \mathbf{n}) + \frac{R' u^s}{R\alpha} (\boldsymbol{\nu} \otimes \boldsymbol{\nu} - \boldsymbol{\tau} \otimes \boldsymbol{\tau}) + \kappa u^s \mathbf{n} \otimes \boldsymbol{\tau} + \partial_h u_\tau \boldsymbol{\tau} \otimes \mathbf{n}, \\ 2\mathbf{D}[\mathbf{u}] &= \frac{(2R u^s)'}{R\alpha} (\boldsymbol{\tau} \otimes \boldsymbol{\tau} - \mathbf{n} \otimes \mathbf{n}) + \frac{2R' u^s}{R\alpha} (\boldsymbol{\nu} \otimes \boldsymbol{\nu} - \boldsymbol{\tau} \otimes \boldsymbol{\tau}) \\ &\quad + (\partial_h u_\tau + \kappa u^s) (\mathbf{n} \otimes \boldsymbol{\tau} + \boldsymbol{\tau} \otimes \mathbf{n}) \end{aligned}$$

on Γ . The stress tensor $\mathbf{f} = -p\mathbf{n} + 2\mu\mathbf{D}[\mathbf{u}] \cdot \mathbf{n}$ on Γ is then found as

$$\mathbf{f} = -\left(p + \frac{2\mu}{R\alpha}(Ru^s)'\right)\mathbf{n} + \mu(\partial_h u_\tau + \kappa u^s)\boldsymbol{\tau}.$$

In particular, taking the tangential and normal projections of \mathbf{f} , we obtain

$$\frac{2\mu}{R\alpha}(Ru^s)' = -f_n - p, \quad \partial_h u_\tau = \frac{1}{\mu}f_\tau - \kappa u^s,$$

which, used in (C.4), establishes the first part of the lemma. Using $(u^s, U) = (0, 1)$ in this result then yields the second part.

Reproducibility of computational results. This paper has been awarded the “SIAM Reproducibility Badge: Code and Data Available” as a recognition that the authors have followed reproducibility principles valued by SISC and the scientific computing community. Code and data that allow readers to reproduce the results in this paper are available at <https://github.com/ruowenliu/axisym3Dswimmer/> and in the supplementary materials (`axisym3Dswimmer-main.zip` [local/web 8.78MB]), linked from the main article webpage.

REFERENCES

- [1] F. ALOUGES, A. DESIMONE, AND L. HELTAI, *Numerical strategies for stroke optimization of axisymmetric microswimmers*, Math. Models Methods Appl. Sci., 21 (2011), pp. 361–387, <https://doi.org/10.1142/S0218202511005088>.
- [2] J. L. ANDERSON, *Colloid transport by interfacial forces*, Annu. Rev. Fluid Mech., 21 (1989), pp. 61–99.
- [3] J. R. BLAKE, *A spherical envelope approach to ciliary propulsion*, J. Fluid Mech., 46 (1971), pp. 199–208, <https://doi.org/10.1017/S002211207100048X>.
- [4] M. BONNET, R. LIU, AND S. VEERAPANENI, *Shape optimization of Stokesian peristaltic pumps using boundary integral methods*, Adv. Comput. Math., 46 (2020), 18, <https://doi.org/10.1007/s10444-020-09761-7>.
- [5] M. BONNET, R. LIU, S. VEERAPANENI, AND H. ZHU, *Shape optimization of peristaltic pumps transporting rigid particles in Stokes flow*, SIAM J. Sci. Comput., 45 (2023), pp. B78–B106, <https://doi.org/10.1137/21M144863X>.
- [6] J.-M. BOUROT, *On the numerical computation of the optimum profile in Stokes flow*, J. Fluid Mech., 65 (1974), pp. 513–515, <https://doi.org/10.1017/S0022112074001510>.
- [7] J. BREMER, Z. GIMBUTAS, AND V. ROKHLIN, *A nonlinear optimization procedure for generalized Gaussian quadratures*, SIAM J. Sci. Comput., 32 (2010), pp. 1761–1788, <https://doi.org/10.1137/080737046>.
- [8] C. BRENNEN AND H. WINET, *Fluid mechanics of propulsion by cilia and flagella*, Annu. Rev. Fluid Mech., 9 (1977), pp. 339–398, <https://doi.org/10.1146/annurev.fl.09.010177.002011>.
- [9] F. BREZZI AND M. FORTIN, *Mixed and Hybrid Element Methods*, Springer, 1991.
- [10] J. ELGETI, R. G. WINKLER, AND G. GOMPPER, *Physics of microswimmers—single particle motion and collective behavior: A review*, Rep. Prog. Phys., 78 (2015), 056601, <https://doi.org/10.1088/0034-4885/78/5/056601>.
- [11] R. GOLESTANIAN, T. B. LIVERPOOL, AND A. AJDARI, *Designing phoretic micro-and nanoswimmers*, New J. Phys., 9 (2007), 126, <https://doi.org/10.1088/1367-2630/9/5/126>.
- [12] H. GUO, H. ZHU, R. LIU, M. BONNET, AND S. VEERAPANENI, *Optimal ciliary locomotion of axisymmetric microswimmers*, J. Fluid Mech., 927 (2021), A22, <https://doi.org/10.1017/jfm.2021.744>.
- [13] H. GUO, H. ZHU, R. LIU, M. BONNET, AND S. VEERAPANENI, *Optimal slip velocities of microswimmers with arbitrary axisymmetric shapes*, J. Fluid Mech., 910 (2021), A26, <https://doi.org/10.1017/jfm.2020.969>.
- [14] A. HENROT AND M. PIERRE, *Shape Variation and Optimization. A Geometrical Analysis*, European Mathematical Society, 2018.
- [15] M. HINZE, R. PINNAU, M. ULRICH, AND S. ULRICH, *Optimization with PDE Constraints*, Math. Model. Theory Appl. 23, Springer, 2008.

- [16] E. LAUGA AND T. R. POWERS, *The hydrodynamics of swimming microorganisms*, Rep. Prog. Phys., 72 (2009), 096601, <https://doi.org/10.1088/0034-4885/72/9/096601>.
- [17] A. M. LESHANSKY, O. KENNETH, O. GAT, AND J. E. AVRON, *A frictionless microswimmer*, New J. Phys., 9 (2007), 145, <https://doi.org/10.1088/1367-2630/9/5/145>.
- [18] J. LI, B. ESTEBAN-FERNÁNDEZ DE ÁVILA, W. GAO, L. ZHANG, AND J. WANG, *Micro/nanorobots for biomedicine: Delivery, surgery, sensing, and detoxification*, Sci. Robot., 2 (2017), eaam6431, <https://doi.org/10.1126/scirobotics.aam6431>.
- [19] M. J. LIGHTHILL, *On the squirming motion of nearly spherical deformable bodies through liquids at very small Reynolds numbers*, Comm. Pure Appl. Math., 5 (1952), pp. 109–118, <https://doi.org/10.1002/cpa.3160050201>.
- [20] S. MICHELIN AND E. LAUGA, *Efficiency optimization and symmetry-breaking in a model of ciliary locomotion*, Phys. Fluids, 22 (2010), 111901, <https://doi.org/10.1063/1.3507951>.
- [21] T. D. MONTENEGRO-JOHNSON AND E. LAUGA, *The other optimal Stokes drag profile*, J. Fluid Mech., 762 (2015), R3, <https://doi.org/10.1017/jfm.2014.673>.
- [22] J. L. MORAN AND J. D. POSNER, *Phoretic self-propulsion*, Annu. Rev. Fluid Mech., 49 (2017), pp. 511–540, <https://doi.org/10.1146/annurev-fluid-122414-034456>.
- [23] J. NOCEDAL AND S. J. WRIGHT, *Numerical optimization*, 2nd ed., Springer, 2006.
- [24] T. PEDLEY, *Spherical squirmers: Models for swimming micro-organisms*, IMA J. Appl. Math., 81 (2016), pp. 488–521, <https://doi.org/10.1093/imamat/hxw030>.
- [25] O. PIRONNEAU, *On optimum profiles in Stokes flow*, J. Fluid Mech., 59 (1973), pp. 117–128, <https://doi.org/10.1017/S002211207300145X>.
- [26] S. K. VEERAPANENI, D. GUEYFIER, G. BIROS, AND D. ZORIN, *A numerical method for simulating the dynamics of 3d axisymmetric vesicles suspended in viscous flows*, J. Comput. Phys., 228 (2009), pp. 7233–7249, <https://doi.org/10.1016/j.jcp.2009.06.020>.
- [27] A. VILFAN, *Optimal shapes of surface slip driven self-propelled microswimmers*, Phys. Rev. Lett., 109 (2012), 128105, <https://doi.org/10.1103/PhysRevLett.109.128105>.
- [28] S. W. WALKER AND E. E. KEAVENY, *Analysis of shape optimization for magnetic microswimmers*, SIAM J. Control Optim., 51 (2013), pp. 3093–3126, <https://doi.org/10.1137/110845823>.
- [29] M. ZABARANKIN AND A. MOLYBOHA, *Three-dimensional shape optimization in stokes flow problems*, SIAM J. Appl. Math., 70 (2010), pp. 1788–1809, <https://doi.org/10.1137/090751578>.